Transformation of a skyrmionium to a skyrmion through the thermal annihilation of the inner skyrmion

Anjie Jiang,[1] Yan Zhou,[1,*] Xichao Zhang,[2] and Masahito Mochizuki[2]
[1]*School of Science and Engineering, The Chinese University of Hong Kong, Shenzhen, Guangdong 518172, China*
[2]*Department of Applied Physics, Waseda University, Okubo, Shinjuku-ku, Tokyo 169-8555, Japan*

(Received 24 August 2023; revised 15 November 2023; accepted 3 January 2024; published 4 March 2024)

Skyrmioniums are doughnutlike topological spin textures in chiral magnets, which are able to move with zero skyrmion Hall effect. The annihilation of a skyrmionium involves the topological transition through singularity formation at the continuum level. Here we analytically and numerically study a type of thermal annihilation of a skyrmionium under the framework of micromagnetism. The skyrmionium initially exists in an ultrathin ferromagnetic film in the exchange-dominated regime and is stabilized under a uniform perpendicular magnetic field. The thermal annihilation of the "skyrmion" inside the skyrmionium results in the transformation of the skyrmionium to a skyrmion. We derive an analytical formula in the Arrhenius form describing the annihilation rate of this process. We find that the analytical solutions agree well with the micromagnetic simulation results. Besides, from the large deviation point of view, we derive the dynamical path for the collapse of a skyrmionium. Our results are useful for understanding the thermal stability of skyrmioniums and may lead to spintronic applications based on the thermal manipulation of skyrmioniums.

DOI: 10.1103/PhysRevResearch.6.013229

I. INTRODUCTION

Magnetic skyrmions, as shown in Fig. 1, are topologically protected nanoscale spin solitions [1–7]. Skyrmions have many good properties including low threshold current and high mobility, which suggests a promising future for skyrmions in information storage and processing [6–22]. However, due to their nonzero topological charge, skyrmions experience topology-dependent Magnus forces that occur under certain external stimulus; for instance, spin-polarized currents may lead to the deflection of a skyrmion during its motion. This effect is known as the skyrmion Hall effect, which may affect the performance of some applications based on the in-line motion of skyrmions [21–24].

Skyrmionium, or 2π twisted skyrmion, is another stable solution in certain parameter regions [2,25–33]. A skyrmionium, as shown in Fig. 1, can be considered as a combination of two skyrmions with opposite topological charges. The total topological charge of a skyrmionium is zero. Hence, skyrmioniums could show zero skyrmion Hall effect, which has been confirmed experimentally [34]. However, under certain conditions, skyrmioniums may exhibit the skyrmion Hall effect, suggesting their additional potential in sensing applications [35,36]. In addition, skyrmioniums could have other advantages like an even higher mobility than skyrmions under certain conditions [36–39]. Therefore, many studies have suggested skyrmioniums as an alternative candidate building block for spintronic applications [34,36–46]. Skyrmioniums can be distinguished from the ferromagnetic state under nonvanishing Dzyaloshinskii-Moriya interactions [47]. Hence, their annihilation involves topological change, as confirmed by several simulation and experimental studies [26,27,36–38,41,43,48–50].

The stability of skyrmioniums is essential for the applications of skyrmioniums as a nonvolatile information carrier and as a sensor in spintronic information storage and processing devices [34,36–46]. With the assistance of thermal noise, topologically protected nanoscale magnetic structures like skyrmions and skyrmioniums can generate, evolve in Brownian particlelike dynamics driven by thermal fluctuations, respond to external stimulus like spin waves, and annihilate through topological transition under various conditions [8–14,26,50–62]. Especially, the stability of skyrmioniums has been studied through the geodesic nudged elastic band (GNEB) method based atomic spin simulation and extension of harmonic transition state theory of skyrmions [26,50,59]. In this work, we focus on the annihilation process from a skyrmionium to a skyrmion by annihilating the inner circular domain wall of a skyrmionium (i.e., the inner one of the two skyrmions that construct a skyrmionium), which is a type of annihilation of a skyrmionium. For other definitions of the annihilation transitions from a skyrmionium to the ferromagnetic state, they could be a combination of our studied case and the annihilation of a single isolated skyrmion. The latter has been studied in Ref. [63].

In this paper, we employ the method developed by Bernand-Mantel, Muratov, and Slastikov [63] and get a coarse-grained description on the annihilation of

*zhouyan@cuhk.edu.cn

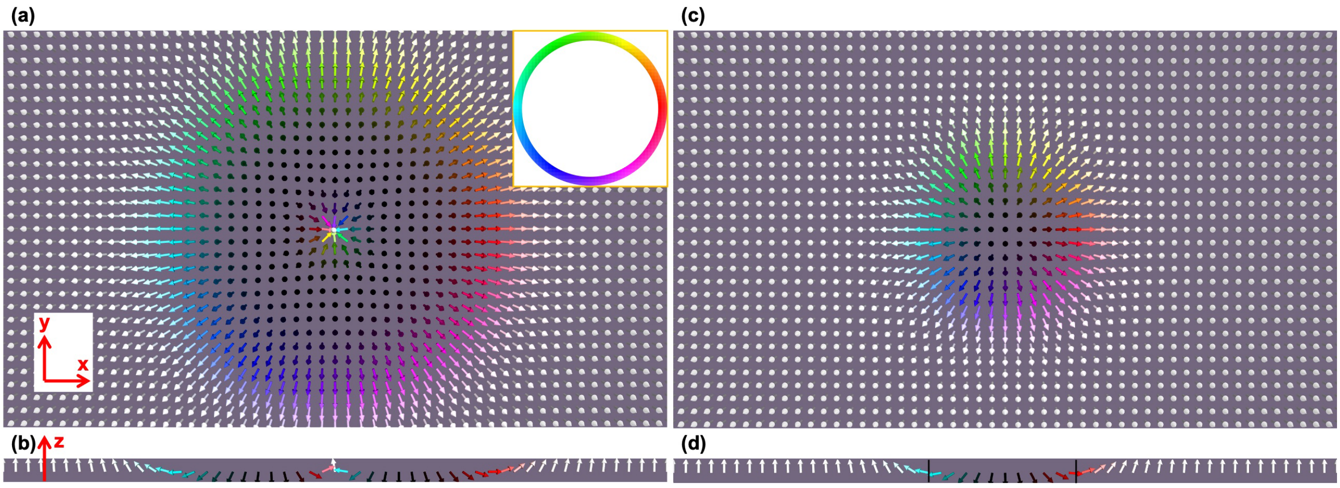

FIG. 1. Magnetization profile for $A = 15$ pJ m^{-1}, $D = 3.115$ mJ m^{-2}, $K_u = 0.8$ MJ m^{-3}, $M_s = 0.58$ MA m^{-1} and $B_{ext} = 0$ T. Figures are colored with respect to the standard hue, saturation, and luminance (HSL) color space. HSL color wheel is given at the top right corner of panels (a). The length scale remains identical within the same figure. The reference frame is indicated with red arrows. (a) Vertical view for a skyrmionium. (b) Side view for a skyrmionium. (c) Vertical view for a skyrmion. (d) Side view for a skyrmion. The black lines indicate the radius ρ_{Sk}.

skyrmioniums. We first use the stochastic Landau-Lifshitz-Gilbert (sLLG) equation to derive some integral identities with respect to the fundamental continuous symmetry groups of the exchange energy. In the exchange-dominated regime, we apply the reduced description of skyrmionium and conduct finite-dimensional reduction of the stochastic skyrmionium dynamics. Consequently, we get a system of stochastic ordinary differential equations for parameters of the magnetic profile of the skyrmionium. By interpreting the skyrmionium annihilation events as "capture by an attractor" at microscale [63], we derive an analytical equation describing a type of thermal annihilation of the skyrmionium and the dynamical path for the collapse from a skyrmionium into a skyrmion. Our method requires low computational cost and few microscopic details to get a satisfying approximation for a type of annihilation of skyrmioniums by offering a reasonable ansatz. Our results could be useful for the thermal manipulation of skyrmioniums in spintronic applications.

II. MODEL

A. Energy

We first give the energy in the continuum magnetization framework in SI units [3,64,65]:

$$\begin{aligned} E = &\frac{A}{M_s^2}\int_{\Omega\times(0,d)}|\nabla \boldsymbol{M}|^2 dV + \frac{K_u}{M_s^2}\int_{\Omega\times(0,d)}|\boldsymbol{M}_{\text{plane}}|^2 dV \\ &+\frac{\mu_0}{8\pi}\int_{\mathbb{R}^3}\int_{\mathbb{R}^3}\frac{\nabla\cdot\boldsymbol{M}(\boldsymbol{r})\nabla\cdot\boldsymbol{M}(\boldsymbol{r}')}{|\boldsymbol{r}-\boldsymbol{r}'|}dV\,dV' \\ &+\frac{Dd}{M_s^2}\int_{\Omega}(\mathcal{M}_z\nabla\cdot\mathcal{M}_{\text{plane}} - \mathcal{M}_{\text{plane}}\cdot\nabla\mathcal{M}_z)dS \\ &+B_{\text{ext}}\int_{\Omega\times(0,d)}(M_s - \boldsymbol{M}_z)dV, \end{aligned} \tag{1}$$

where the terms in the right-hand side of Eq. (1) are the exchange energy, the magnetocrystalline anisotropy energy, the magnetostatic energy, the interfacial Dzyaloshinskii-Moriya interaction (DMI) energy, and the Zeeman energy, respectively [66,67]. $\Omega \subseteq \mathbb{R}^2$ is a two-dimensional domain describing the thin film of thickness d in the plane. $\boldsymbol{M}(\boldsymbol{r}) : \Omega\times(0,d)\mapsto\mathbb{R}^3$ is the magnetization vector at position $\boldsymbol{r}$ which has fixed length M_s. $\boldsymbol{M} = (\boldsymbol{M}_{\text{plane}}, \boldsymbol{M}_z)$ is extended by zero to whole $\mathbb{R}^3$ in the definition of the stray field energy. $\mathcal{M} = (\mathcal{M}_{\text{plane}}, \mathcal{M}_z)$ is the magnetization vector at one of the surfaces. A, K_u, D, μ_0, and B_{ext} are the exchange stiffness, the perpendicular magnetocrystalline anisotropy constant, the interfacial DMI coefficient, the vacuum permeability, and the perpendicular magnetic field. The energy reference is the single domain state of $\boldsymbol{M}_z = M_s$.

In the following, we consider a sufficiently large two-dimensional film for simplicity. Then $\Omega = \mathbb{R}^2$, $\boldsymbol{M}$ is uniform in thickness direction, and the magnetostatic energy can be included by correcting K_u into the effective anisotropy constant $K_{\text{eff}} = K_u - \frac{\mu_0 M_s^2}{2}$ [68]. To simplify the calculation, the exchange length $l_{ex} = \sqrt{\frac{2A}{\mu_0 M_s^2}}$ is used as the length unit [69], $E_0 = 2Ad$ is used as the energy unit, and $\boldsymbol{m} = \frac{\boldsymbol{M}}{M_s}$, $Q = \frac{2K_u}{\mu_0 M_s^2}$, and $\kappa = \sqrt{\frac{2D^2}{\mu_0 M_s^2 A}}$ are defined. From the definition, it is trivial that $Q > 1$ is concerned. $\epsilon = \frac{k_B T}{2Ad}$ is defined with the Boltzmann constant k_B and the temperature T. Equation (1) becomes

$$\begin{aligned} E(\boldsymbol{m}) = &\frac{1}{2}\int_{\mathbb{R}^2}\bigg[|\nabla\boldsymbol{m}|^2 + (Q-1)|\boldsymbol{m}_{\text{plane}}|^2 \\ &- 2\kappa\boldsymbol{m}_{\text{plane}}\cdot\nabla\boldsymbol{m}_z + \frac{2B_{\text{ext}}}{\mu_0 M_s}(1-\boldsymbol{m}_z)\bigg]dS. \end{aligned} \tag{2}$$

In this work, we use the stochastic sLLG equation to describe the continous magnetization dynamics in the ultrathin ferromagnetic film at finite temperature [64,70–72]:

$$\frac{\partial \boldsymbol{m}}{\partial t} = -\boldsymbol{m} \times \boldsymbol{h}_{\rm eff} + \alpha\left(\boldsymbol{m} \times \frac{\partial \boldsymbol{m}}{\partial t}\right), \tag{3}$$

where α is the dimensionless Gilbert damping parameter and $\tau_0 = \frac{1}{\gamma\mu_0 M_s}$ is used as the time unit, with γ being the gyromagnetic ratio. The effective field is $\boldsymbol{h}_{\rm eff} = -\frac{\delta E(\boldsymbol{m})}{\delta \boldsymbol{m}} + \sqrt{2\alpha\epsilon}\boldsymbol{\xi}$, where $\boldsymbol{\xi}(\boldsymbol{r},t)$ is a suitable regularization of a three-dimensional delta-correlated spatiotemporal white noise [70,73].

For convenience, we introduce the polar coordinates so that $\boldsymbol{m} = [\sin\theta\cos\phi, \sin\theta\sin\phi, \cos\theta]$. Then the partial derivative of $\boldsymbol{m}$ over time $\boldsymbol{m}_t$ can be completely described by superposition of two other coordinates $\boldsymbol{p} = [-\sin\phi, \cos\phi, 0] = [\boldsymbol{p}_{\rm plane}, 0]$ and $[\cos\theta\cos\phi, \cos\theta\sin\phi, -\sin\theta]$ forming an orthonomal set with $\boldsymbol{m}$. Considering the sLLG equation in those directions, we have

$$\begin{bmatrix} \alpha & -1 \\ 1 & \alpha \end{bmatrix}\begin{bmatrix} \theta_t \\ \sin(\theta)\phi_t \end{bmatrix} = \begin{bmatrix} \nabla^2\theta - \frac{\sin(2\theta)}{2}(|\nabla\phi|^2 + Q - 1) \\ \sin(\theta)\nabla^2\phi + 2\cos(\theta)\nabla\theta\cdot\nabla\phi \end{bmatrix} + \begin{bmatrix} -\frac{B_{\rm ext}}{\mu_0 M_s}\sin(\theta) + \kappa\sin^2(\theta)\nabla\phi\cdot\boldsymbol{p}_{\rm plane} + \sqrt{2\alpha\epsilon}\eta \\ -\kappa\sin(\theta)\nabla\theta\cdot\boldsymbol{p}_{\rm plane} + \sqrt{2\alpha\epsilon}\zeta \end{bmatrix}, \tag{4}$$

where η and ζ are two independent and delta-correlated spatiotemporal white noises in two space dimensions.

B. Integral identities

Here, we derive several integral identities in an exchange-dominated regime from sLLG equations in polar form with respect to symmetry groups.

Consider rotations by multiplying Eq. (4) by $[0, \sin\theta]$ and integrate over space. Since the small thermal noise regime is concerned, we can neglect the Itô corrections and consider the Itô formulation and the Stratonovich formulation equally [74]. Subsequently, the integral identity becomes

$$\begin{aligned} &\int_{\mathbb{R}^2} [\sin(\theta)\theta_t + \alpha\sin^2(\theta)\phi_t + \kappa\sin^2(\theta)\nabla\theta\cdot\boldsymbol{p}_{\rm plane}]dS \\ &= \int_{\mathbb{R}^2} (\sqrt{2\alpha\epsilon}\sin(\theta)\zeta)dS \\ &= \sqrt{2\alpha\epsilon}\left(\int_{\mathbb{R}^2} \sin^2(\theta)dS\right)^{\frac{1}{2}}\dot{W}_1(t), \end{aligned} \tag{5}$$

where $W_1(t)$ is a Wiener process, and $\dot{W}_1(t) = \frac{\partial W_1}{\partial t}$ [75].

Similarly, considering dilations by multiplying Eq. (4) by $\{\nabla\theta\cdot[\boldsymbol{r} - \boldsymbol{r}_0(t)], \sin(\theta)\nabla\phi\cdot[\boldsymbol{r} - \boldsymbol{r}_0(t)]\}$, and integrating over space yields the following equation:

$$\begin{aligned} &\int_{\mathbb{R}^2} \{\nabla\boldsymbol{\theta}\cdot(\boldsymbol{r} - \boldsymbol{r}_0)[\alpha\theta_t - \sin(\theta)\phi]\}dS + \int_{\mathbb{R}^2} \{\nabla\phi\cdot(\boldsymbol{r} - \boldsymbol{r}_0)[\alpha\sin^2(\theta)\phi_t + \sin(\theta)\theta_t]\}dS \\ &= \int_{\mathbb{R}^2} \left\{\nabla\theta\cdot(\boldsymbol{r} - \boldsymbol{r}_0)\left[(1 - Q)\frac{\sin(2\theta)}{2} - \frac{B_{\rm ext}\sin\theta}{\mu_0 M_s}\right]\right\}dS + \int_{\mathbb{R}^2} [\nabla\theta\cdot(\boldsymbol{r} - \boldsymbol{r}_0)\kappa\sin^2(\theta)\nabla\phi\cdot\boldsymbol{p}_{\rm plane}]dS \\ &\quad - \int_{\mathbb{R}^2} [\sin^2(\theta)\nabla\phi\cdot(\boldsymbol{r} - \boldsymbol{r}_0)\kappa\nabla\theta\cdot\boldsymbol{p}_{\rm plane}]dS + \sqrt{\int_{\mathbb{R}^2} [|\nabla\theta\cdot(\boldsymbol{r} - \boldsymbol{r}_0)|^2 + |\sin(\theta)\nabla\phi\cdot(\boldsymbol{r} - \boldsymbol{r}_0)|^2]dS\sqrt{2\alpha\epsilon}\dot{W}_2(t)}, \end{aligned} \tag{6}$$

where $W_2(t)$ is another Wiener process. Here $\boldsymbol{r}_0(t)$ can take an arbitrary form and will be specified later.

Similarly, considering translations by multiplying Eq. (4) by $[\theta_x, \sin(\theta)\phi_x]$ and $[\theta_y, \sin(\theta)\phi_y]$, where subscripts x and y represent partial derivatives over those coordinates, respectively, and integrating over space yields

$$\begin{aligned} &\int_{\mathbb{R}^2} \{\theta_x[\alpha\theta_t - \sin(\theta)\phi_t] + \phi[\alpha\sin^2(\theta)\phi_t + \sin(\theta)\theta_t]\}dS \\ &= \int_{\mathbb{R}^2} \left\{\theta_x\left[(1 - Q)\frac{\sin(2\theta)}{2} - \frac{B_{\rm ext}\sin(\theta)}{\mu_0 M_s}\right]\right\}dS + \int_{\mathbb{R}^2} \left[\theta_x\kappa\sin^2(\theta)\nabla\phi\cdot\boldsymbol{p}_{\rm plane} - \sin^2(\theta)\kappa\phi_x\nabla\theta\cdot\boldsymbol{p}_{\rm plane}\right]dS \\ &\quad + \sqrt{\int_{\mathbb{R}^2} [|\theta_x|^2 + |\sin(\theta)\phi_x|^2]dS} \times \sqrt{2\alpha\epsilon}\dot{W}_3(t); \end{aligned} \tag{7}$$

$$\begin{aligned} &\int_{\mathbb{R}^2} \{\theta_y[\alpha\theta_t - \sin(\theta)\phi_t] + \phi_y[\alpha\sin^2(\theta)\phi_t + \sin(\theta)\theta_t]\}dS \\ &= \int_{\mathbb{R}^2} \left\{\theta_y\left[(1 - Q)\frac{\sin(2\theta)}{2} - \frac{B_{\rm ext}\sin(\theta)}{\mu_0 M_s}\right]\right\}dS + \int_{\mathbb{R}^2} \left[\theta_y\kappa\sin^2(\theta)\nabla\phi\cdot\boldsymbol{p}_{\rm plane} - \sin^2(\theta)\kappa\phi_y\nabla\theta\cdot\boldsymbol{p}_{\rm plane}\right]dS \\ &\quad + \sqrt{\int_{\mathbb{R}^2} [|\theta_y|^2 + |\sin(\theta)\phi_y|^2]dS} \times \sqrt{2\alpha\epsilon}\dot{W}_4(t), \end{aligned} \tag{8}$$

where $W_3(t)$ and $W_4(t)$ are two other Wiener processes.

C. Reduced profile

Here we are examining the profile of a skyrmionium. We noted that the associated Euler-Lagrange equation of micromagnetic energy for skyrmioniums has the same form as that for skyrmions. The only difference is the boundary conditions: $\theta(0) = 0(\pi)$ and $\theta(\infty) = \pi(0)$ for skyrmions, and $\theta(0) = 0(2\pi)$ and $\theta(\infty) = 2\pi(0)$ for skyrmioniums. We propose a reduced profile of skyrmioniums from the approximation of the skyrmion profile with the 2π domain wall profile, which has been verified to a satisfying accuracy both by simulations and by experiments [76–78]. The 2π domain wall profile derived by Braun can be considered as a superposition of twisted π domain wall pairs [79]. Similarly we could verify that the 4π domain wall profile can be considered as a superposition of twisted 2π domain wall pairs, which has the form

$$\theta_{4\pi}(z) = \theta_{2\pi}\left(-\frac{z}{\delta_b} + R_b\right) + \theta_{2\pi}\left(-\frac{z}{\delta_b} - R_b\right), \tag{9}$$

where δ_b and R_b are coefficients that can be identified later. Following the analogy, we approximate the skyrmionium profile with the 4π domain wall profile. Furthermore, we stick with the approximate equivalence between the skyrmion profile and the 2π domain wall profile. Then the skyrmionium profile can be considered as a superposition of the skyrmion profile pair approximately.

For simplicity, we choose the Belavin-Polyakov profile as the skyrmion profile θ_{Sk} at the core [80,81]:

$$\theta_{Sk}(r) \backsimeq 2\arctan\left(\frac{r}{\rho_{Sk}}\right), \tag{10}$$

where ρ_{Sk} is the radius of the skyrmion.

Without loss of generality, we can set $\rho_{Sk} = 1$ and vary the parameters δ_{Sk} and R_{Sk} to get all possible profiles. Define $\mathcal{A} = \frac{\delta_{Sk}(1+R_{Sk}^2)}{2}$ and $\mathcal{B} = \frac{1}{2\delta_{Sk}}$, the profile becomes

$$\begin{aligned}\theta(r) &\backsimeq \theta_{Sk}\left(-\frac{r}{\delta_{Sk}} + R_{Sk}\right) + \theta_{Sk}\left(-\frac{r}{\delta_{Sk}} - R_{Sk}\right)\\ &\backsimeq 2\arctan\left(\frac{r}{\mathcal{A} - \mathcal{B}r^2}\right) + 2\pi n,\end{aligned} \tag{11}$$

where $n \in \mathbb{Z}$ are some integers that make the curve smooth.

While at the tail, the Euler-Lagrange equation can be approximately linearized, yielding an exponentially decaying profile on the scale of $\mathcal{L}_s = (\sqrt{Q - 1 + \frac{B_{ext}}{\mu_0 M_s}})^{-1}$ (in l_{ex}) [82]:

$$[2\pi - \theta(r)] \propto K_1\left(\frac{r}{\mathcal{L}_s}\right), \tag{12}$$

where $K_1(z)$ is the modified Bessel function of the second kind, which is approximately $K_1(\frac{r}{\mathcal{L}_s}) \approx e^{-\frac{r}{\mathcal{L}_s}} r^{-\frac{1}{2}}$.

It is expected that the profile would approximately stablize on the timescale $\tau_{core} \backsim \mathcal{A}^2$ at the core and $\tau_{tail} \backsim \mathcal{L}_s^2$ at the tail [63]. Hence, on the timescale $\tau_{tail} \gtrsim \tau_{core}$, we may consider the dynamical profile approximately as the profile at the core.

For convenience, we consider the center of the skyrmionium to be $\boldsymbol{r}_0(t)$, and we consider the polar coordinates with respect to the center $[r, \psi]$ to be $\boldsymbol{r} = \boldsymbol{r}_0 + [r\cos\psi, r\sin\psi]$. Both at the core and at the tail, we have

$$\phi(\boldsymbol{r}, t) = \arg[\boldsymbol{r} - \boldsymbol{r}_0(t)] + \varphi(t) - \pi, \tag{13}$$

where $\varphi(t)$ is some fixed angle with respect to the structure, which can be interpreted as the rotation angle of the skyrmionium here.

To check the accuracy of the approximation, we calculate the energy and compare it with that calculated from the profile of the direct numerical solution of the Euler-Lagrange equation associated with the micromagnetic energy by the shooting method [83]. For convenience, we use an alternative object in the comparison, the energy of the skyrmionium calculated by MUMAX3 with the Bogacki-Shampine method [84,85]. We first use the radius where $\theta = \pi$, which corresponds to $r_\pi = \sqrt{\frac{\mathcal{A}}{\mathcal{B}}}$, to calibrate the parameters. We then identify δ_{Sk} and R_{Sk} directly by calculating the energy and identifying the energy minima under the contraint of r_π. Note that here we use the core profile to as far as $2r_\pi$ to better characterize skyrmioniums, and we choose a suitable tail profile for the rest area so the profile remains continuous. We varied the parameters and confirmed in Appendix B that the energy difference is within 26% in the selected parameter space. In comparison with the 17% energy difference limit for the Belavin-Polyakov profile by Bernand-Mantel *et al.* [63], we have verified our approximation.

D. Finite-dimensional reduction

Here we substitute the profile into the integral identities and introduce $\mathcal{L}$ as the cutoff length in integrals with logarithmic divergences. We also checked that the Wiener processes are mutually independent to leading order via the correlators. Then, we define the rotated Wiener processes $\tilde{W}_1 = -\frac{\alpha W_1 - W_2}{\sqrt{1+\alpha^2}}$, $\tilde{W}_2 = -\frac{W_1 + \alpha W_2}{\sqrt{1+\alpha^2}}$, $\tilde{W}_3 = -\frac{\alpha W_3 + W_4}{\sqrt{1+\alpha^2}}$, and $\tilde{W}_4 = -\frac{\alpha W_4 - W_3}{\sqrt{1+\alpha^2}}$, which are also mutually independent. After some approximations, we have

$$\begin{aligned}\frac{d}{dt}\begin{bmatrix}\ln\mathcal{A}\\ \varphi\end{bmatrix} &= \sqrt{\frac{\alpha\epsilon}{4\pi\mathcal{D}^2(1+\alpha^2)\ln\left(\frac{\mathcal{L}}{\mathcal{C}}\right)}}\begin{bmatrix}\dot{\tilde{W}}_1\\ \dot{\tilde{W}}_2\end{bmatrix}\\ &\quad - \frac{1}{1+\alpha^2}\begin{bmatrix}-1 & \alpha\\ \alpha & 1\end{bmatrix}\\ &\quad \times \begin{bmatrix}\frac{\mathcal{D}\kappa\sin\varphi}{2\mathcal{C}^2\ln\left(\frac{\mathcal{L}}{\mathcal{C}}\right)}\\ \left|\frac{1+2\mathcal{AB}}{1-2\mathcal{AB}}\right|(Q-1) - \frac{B_{ext}}{\mu_0 M_s} - \frac{\mathcal{D}\kappa\cos\varphi}{2\mathcal{C}^2\ln\left(\frac{\mathcal{L}}{\mathcal{C}}\right)}\end{bmatrix},\end{aligned} \tag{14}$$

where $\mathcal{C}^2 = \frac{\mathcal{A}^2}{1-2\mathcal{AB}}$ and $\mathcal{D} = \frac{\mathcal{A}}{1-2\mathcal{AB}}$ are defined forconvenience. Note that Eq. (14) only applies to the case with $\mathcal{D} > 0$, or with $\mathcal{L}$ limited so some integrals remain convergent:

$$\frac{d}{dt}\begin{bmatrix}x_0\\ y_0\end{bmatrix} = \sqrt{\frac{\alpha\epsilon\mathcal{C}^2}{2\pi(1+\alpha^2)\mathcal{D}^2}}\begin{bmatrix}\dot{\tilde{W}}_3\\ \dot{\tilde{W}}_4\end{bmatrix}, \tag{15}$$

where $\boldsymbol{r}_0 = (x_0, y_0)$. Note that the translational degree of freedom decouples from the structural degree of freedom, yielding a diffusivity coefficient, $D_{eff} = \frac{\alpha\epsilon\mathcal{C}^2}{4\pi(1+\alpha^2)\mathcal{D}^2}$.

Practically, a reflecting boundary condition at some $\mathcal{L}_0 < \mathcal{L}$ is applied, and we set $\ln(\frac{\mathcal{L}}{\mathcal{C}})$ to a constant Λ, taking its leading order. In addition, we introduce $[\bar{x}, \bar{y}] = \mathcal{A}[\cos\varphi, \sin\varphi]$.

Without loss of generality, we denote the suitably rotated Wiener processes as W_1 and W_2. Equation (14) becomes

$$d\bar{x} = \frac{\frac{\alpha\kappa}{2\Lambda} - \mathcal{Q}\alpha\bar{x} + \mathcal{Q}\bar{y}}{1+\alpha^2}dt + \sqrt{\frac{\alpha\bar{\epsilon}}{4\pi(1+\alpha^2)\Lambda}}dW_1, \quad (16)$$

$$d\bar{y} = \frac{\frac{\kappa}{2\Lambda} - \mathcal{Q}\bar{x} - \alpha\mathcal{Q}\bar{y}}{1+\alpha^2}dt + \sqrt{\frac{\alpha\bar{\epsilon}}{4\pi(1+\alpha^2)\Lambda}}dW_2, \quad (17)$$

where $\mathcal{Q} = (Q-1)|\frac{1+2\mathcal{AB}}{1-2\mathcal{AB}}| - \frac{B_{\text{ext}}}{\mu_0 M_s}$ and $\bar{\epsilon} = \frac{\mathcal{A}^2}{\mathcal{D}^2}\epsilon$. Hence, the associated Fokker-Planck equation is

$$\begin{aligned}(1+\alpha^2)p_t =& \left[p\left(-\frac{\alpha\kappa}{2\Lambda} + \mathcal{Q}\alpha\bar{x} - \mathcal{Q}\bar{y}\right)\right]_{\bar{x}} \\ &+ \left[p\left(-\frac{\kappa}{2\Lambda} + \mathcal{Q}\bar{x} + \alpha\mathcal{Q}\bar{y}\right)\right]_{\bar{y}} \\ &+ \frac{\alpha\bar{\epsilon}}{8\pi\Lambda}(p_{\bar{x}\bar{x}} + p_{\bar{y}\bar{y}}). \end{aligned} \quad (18)$$

E. Annihilation time

While more sophisticated results can be found by determining r_π with respect to each different $\mathcal{A}$, for simplicity we assume the change of R_{Sk} is negligible during the annihilation, which corresponds to the regime where R_{Sk} is small. Then we may approximately use $\mathcal{A} = \mathcal{E}r_\pi$ with $\mathcal{E} = \frac{\sqrt{1+R_{\text{Sk}}^2}}{2}$ considered to be a constant. Introducing $[\tilde{x}, \tilde{y}] = r_\pi[\cos\varphi, \sin\varphi]$ to Eq. (18) yields the associated Fokker-Planck equation directly regarding the size of the skyrmionium:

$$\begin{aligned}(1+\alpha^2)p_t =& \left[p\left(-\frac{\alpha\tilde{\kappa}}{2\Lambda} + \mathcal{Q}\alpha\tilde{x} - \mathcal{Q}\tilde{y}\right)\right]_{\tilde{x}} \\ &+ \left[p\left(-\frac{\tilde{\kappa}}{2\Lambda} + \mathcal{Q}\tilde{x} + \alpha\mathcal{Q}\tilde{y}\right)\right]_{\tilde{y}} \\ &+ \frac{\alpha\tilde{\epsilon}}{8\pi\Lambda}(p_{\tilde{x}\tilde{x}} + p_{\tilde{y}\tilde{y}}), \end{aligned} \quad (19)$$

where $\tilde{\kappa} = \frac{\kappa}{\mathcal{E}}$ and $\tilde{\epsilon} = \frac{\mathcal{A}^2}{\mathcal{D}^2\mathcal{E}^2}\epsilon$. Introducing complex $\tilde{z} = \tilde{x} + i\tilde{y}$, we have the equilibrium measure

$$p_{\text{eq}}(\tilde{z}) = \frac{4\Lambda\mathcal{Q}}{\tilde{\epsilon}}\exp\left(-\frac{H(\tilde{z})}{\tilde{\epsilon}}\right), \quad (20)$$

where $H(\tilde{z}) = 4\pi\Lambda\mathcal{Q}|\tilde{z} - \tilde{z}_0|^2$ and $\tilde{z}_0 = \frac{\tilde{\kappa}}{2\Lambda\mathcal{Q}}$. The probability of its solution starting at $\tilde{z} = \tilde{z}_0$ to reach $\tilde{z} = 0$ is zero, which agrees with the topological stability of the structure. Therefore, we interpret the annihilation event implicitly. Since topological singularity occurs and continuity breaks down when the size of the structure is small enough [86], we introduce an absorber at $|\tilde{z}| = \delta$ [63]. In atomically thin films, δ is on the order of the film size d. Since the consequential transition without topological protection is spontaneous, we may consider that the energy barrier has been passed during the occurrence of topological rupture.

Then we consider a stationary process in which a particle following Eq. (19) is reinjected into the neighborhood of $\tilde{z}_0$ with the probability $\tilde{g}(\tilde{z})d\tilde{x}d\tilde{y}$ whenever it hits the absorber, where $\tilde{g}(\tilde{z})$ is a positive function whose support contains a small neighborhood of $\tilde{z}_0$ [87]. For small $\tilde{\epsilon}$ cases, the exact form of $\tilde{g}$ is of no concern, since the solution will differ from p_{eq} only around the point closest to $\tilde{z}_0$ on the absorber. For convenience, we introduce $q = \frac{p}{p_{\text{eq}}}$ to the equation describing the stationary process, yielding

$$\begin{aligned}-\frac{C_{\tilde{\epsilon}}\tilde{g}}{p_{\text{eq}}} =& \left(\mathcal{Q}x - \frac{\tilde{\kappa}}{2\Lambda}\right)(\alpha q_{\tilde{x}} + q_{\tilde{y}}) + \mathcal{Q}y(-q_{\tilde{x}} + \alpha q_{\tilde{y}}) \\ &+ \frac{\alpha\tilde{\epsilon}}{8\pi\Lambda}(q_{\tilde{x}\tilde{x}} + q_{\tilde{y}\tilde{y}}), \end{aligned} \quad (21)$$

where x and y are considered independent of $\tilde{x}$ and $\tilde{y}$, $C_{\tilde{\epsilon}}$ is an arbitrary small suitable constant so that the solution integrates to unity over $|\tilde{z}| > \delta$.

Since the closest point is $(\delta, 0)$ [or possibly $(-\delta, 0)$, depending on the sign of $\mathcal{Q}$], q is approximately independent of y and approaches unity for $\tilde{x} \gg \tilde{\epsilon}$. Then consider the following equation in the neighborhood of the closest point, here we consider $(\delta, 0)$ first

$$\left(\mathcal{Q}\delta - \frac{\tilde{\kappa}}{2\Lambda}\right)q_{\tilde{x}} + \frac{\tilde{\epsilon}}{8\pi\Lambda}q_{\tilde{x}\tilde{x}} \approx 0. \quad (22)$$

With the boundary conditions of $q(\delta) = 0$ and $q(\infty) = 1$, the solution in $\tilde{x} \in (\delta, \infty)$ is $q(\tilde{x}) \approx 1 - \exp\{-\frac{8\pi\Lambda}{\tilde{\epsilon}}[\mathcal{Q}\delta - \frac{\tilde{\kappa}}{2\Lambda}](\tilde{x} - \delta)\}$. When $\tilde{\epsilon} \ll \tilde{\kappa}\delta$, the annihilation rate is approximately

$$\begin{aligned}J_\delta \approx& \frac{\alpha\tilde{\epsilon}}{8\pi\Lambda(1+\alpha^2)}\int_{|\tilde{z}|=\delta} p_{\text{eq}}|\nabla q|ds \\ \approx& \frac{\alpha\Lambda\mathcal{Q}}{1+\alpha^2}\left[\frac{\tilde{\kappa}}{2\Lambda} - \mathcal{Q}\delta\right]\left(\frac{8\delta}{\tilde{\epsilon}\tilde{\kappa}}\right)^{\frac{1}{2}}\exp\left(-\frac{H(\delta)}{\tilde{\epsilon}}\right). \end{aligned} \quad (23)$$

In small δ cases as $\tilde{\epsilon} \to 0$, we can further approximate the solution above into

$$J_\delta \approx \frac{\alpha\mathcal{Q}A_\delta}{1+\alpha^2}\left(\frac{2\tilde{\kappa}\delta}{\tilde{\epsilon}}\right)^{\frac{1}{2}}\exp\left(-\frac{\pi\tilde{\kappa}^2}{\tilde{\epsilon}\Lambda\mathcal{Q}}\right), \quad (24)$$

where A_δ corresponds to the reduction in barrier height after introducing the absorber,

$$A_\delta = \exp\left[\frac{4\pi\tilde{\kappa}\delta}{\tilde{\epsilon}}\left(1 - \frac{\Lambda\mathcal{Q}\delta}{\tilde{\kappa}}\right)\right]. \quad (25)$$

Now we consider the $(-\delta, 0)$ case, since it corresponds to $\mathcal{Q} < 0$, we can verify, after altering the sign of both $\mathcal{Q}$ and δ, the final result is the same.

Then we consider the case where $\delta \to 0$. In this case, the solution for Eq. (21) only differs from unity in the diffusive boundary layer around the absorber. Since the advection field is approximately fixed near a small absorber, in a neighborhood of the absorber, after suitable rotation, we approximately have

$$q_{\tilde{x}\tilde{x}} + q_{\tilde{y}\tilde{y}} + \frac{4\pi\tilde{\kappa}\sqrt{1+\alpha^2}}{\alpha\tilde{\epsilon}}q_{\tilde{x}} = 0. \quad (26)$$

For simplicity, we introduce u where $q = 1 - u\exp(-\frac{2\pi\tilde{\kappa}\sqrt{1+\alpha^2}}{\alpha\tilde{\epsilon}}\tilde{x})$. Equation (26) becomes

$$u_{\tilde{x}\tilde{x}} + u_{\tilde{y}\tilde{y}} = \left(\frac{2\pi\tilde{\kappa}\sqrt{1+\alpha^2}}{\alpha\tilde{\epsilon}}\right)^2 u. \quad (27)$$

With the boundary conditions $q(\delta) = 0$ and $q(\infty) = 1$, when $\delta \ll 1$ and $\tilde{\kappa}\delta \ll \tilde{\epsilon}$, the equation above has an approximate solution, $q(\tilde{z}) \approx \ln(\frac{|\tilde{z}_0|}{\delta})/\ln(\frac{\alpha\tilde{\epsilon}\exp(-\gamma_0)}{\pi\delta\tilde{\kappa}\sqrt{1+\alpha^2}}) \approx \ln(\frac{|\tilde{z}_0|}{\delta})/\ln(\frac{\alpha\tilde{\epsilon}\tilde{c}}{\delta\tilde{\kappa}\sqrt{1+\alpha^2}})$,

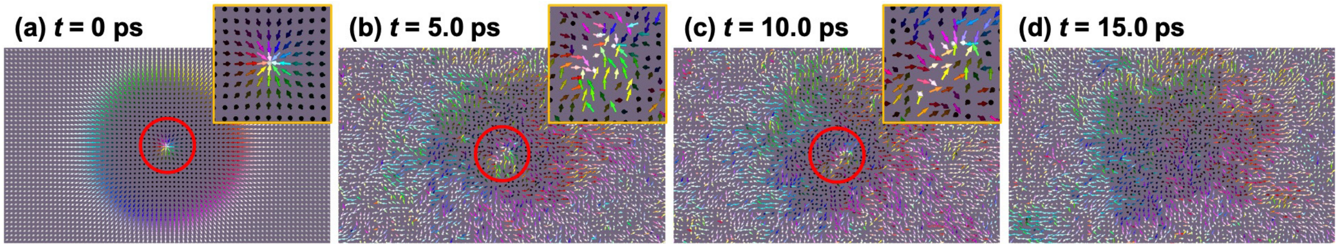

FIG. 2. Annihilation: Magnetization profile for $A = 15$ pJ m^{-1}, $D = 3.115$ mJ m^{-2}, $K_u = 0.8$ MJ m^{-3}, $M_s = 0.58$ MA m^{-1}, $B_{ext} = 0$ T, and $T = 300$ K. Figures are colored with respect to the standard HSL color space. The length scale remains identical within the same figure. The times from panels (a) to (d) are $t = 0$, 5.0, 10.0, and 15.0 ps. The skyrmionium turns into a skyrmion by annihilating the "inner skyrmion", which is confirmed later after the relaxation by topological charge calculation. The red circles highlight the "inner skyrmion." The magnified views of the areas in the circles are given at the top right corner respectively.

where $\gamma_0 \approx 0.5772$ is the Euler-Mascheroni constant and $\bar{c} \approx 0.179$ is a constant [88]. Hence, the annihilation rate is approximately

$$J_\delta \approx \frac{\alpha \mathcal{Q}}{(1+\alpha^2)\ln\left(\frac{\alpha\tilde{\epsilon}\bar{c}}{\delta\tilde{\kappa}\sqrt{1+\alpha^2}}\right)}\exp\left(-\frac{\pi\tilde{\kappa}^2}{\tilde{\epsilon}\Lambda\mathcal{Q}}\right). \tag{28}$$

Similarly we can check that the negative value cases have the same form.

F. Annihilation path

We can obtain the path of skyrmionium annihilation in a small noise regime by minimizing the large deviation action [89]

$$S = \frac{2\pi\Lambda(1+\alpha^2)}{\alpha}\int_0^T \left|\dot{\tilde{z}} + \frac{\alpha+i}{1+\alpha^2}\left[\mathcal{Q}\bar{z} - \frac{\kappa}{2\Lambda}\right]\right|^2 dt. \tag{29}$$

Noted that for simplicity, here we stick with the approximation that $\bar{z} = \mathcal{E}\tilde{z}$. With $\tilde{z}(0) = \tilde{z}_0$, and $\tilde{z}(T) = \delta$ given, let $T \to \infty$, we have the approximated optimal path of the following form when $\delta \ll 1$:

$$\tilde{z}_{\text{opt}} \approx \tilde{z}_0\left\{1 - \exp\left[\frac{\alpha - i}{1+\alpha^2}\mathcal{Q}(t-T)\right]\right\}. \tag{30}$$

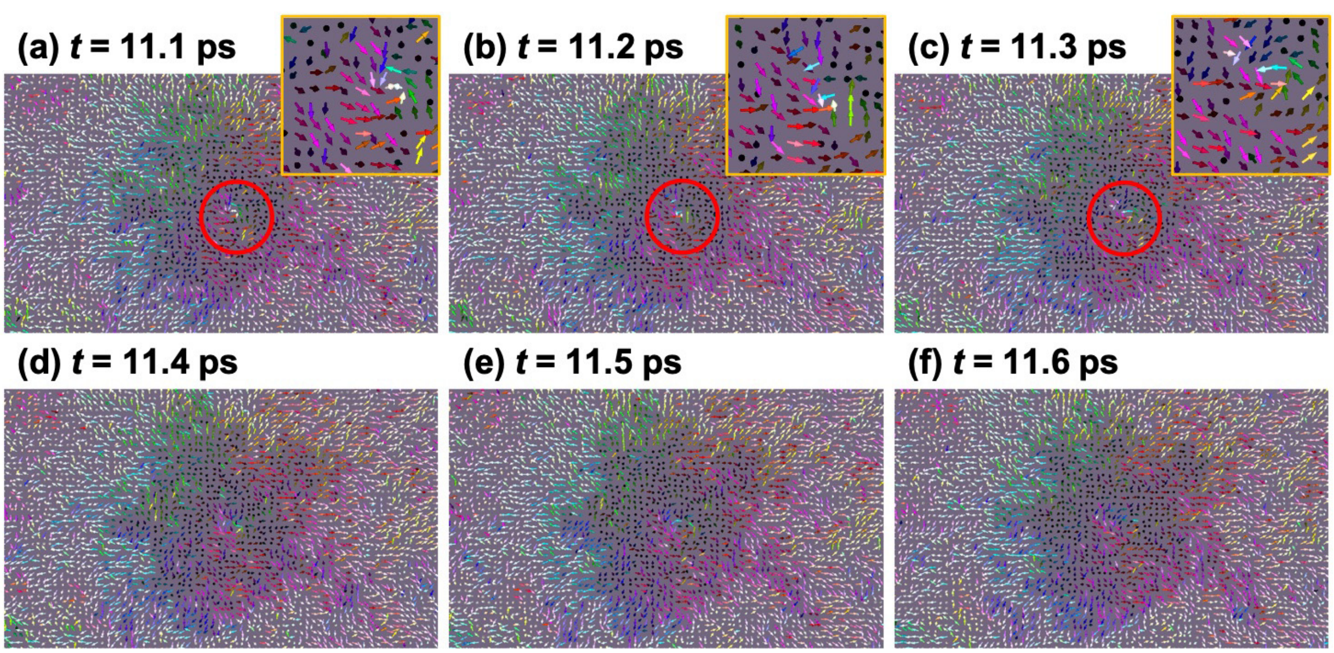

FIG. 3. Transition close-up: Magnetization profile for $A = 15$ pJ m^{-1}, $D = 3.115$ mJ m^{-2}, $K_u = 0.8$ MJ m^{-3}, $M_s = 0.58$ MA m^{-1}, $B_{ext} = 0$ T and $T = 300$ K. Figures are colored with respect to the standard HSL color space. The length scale remains identical within the same figure. The times from panels (a) to (f) are $t = 11.1$, 11.2, 11.3, 11.4, 11.5, and 11.6 ps. The red circles highlight the inner skyrmion. The magnified views of the areas in the circles are given at the top right corner. Notice that while the inner skyrmion has been annihilated and topological change has happened during the process, there are still some minor residual fluctuations inside which will be further mitigated later.

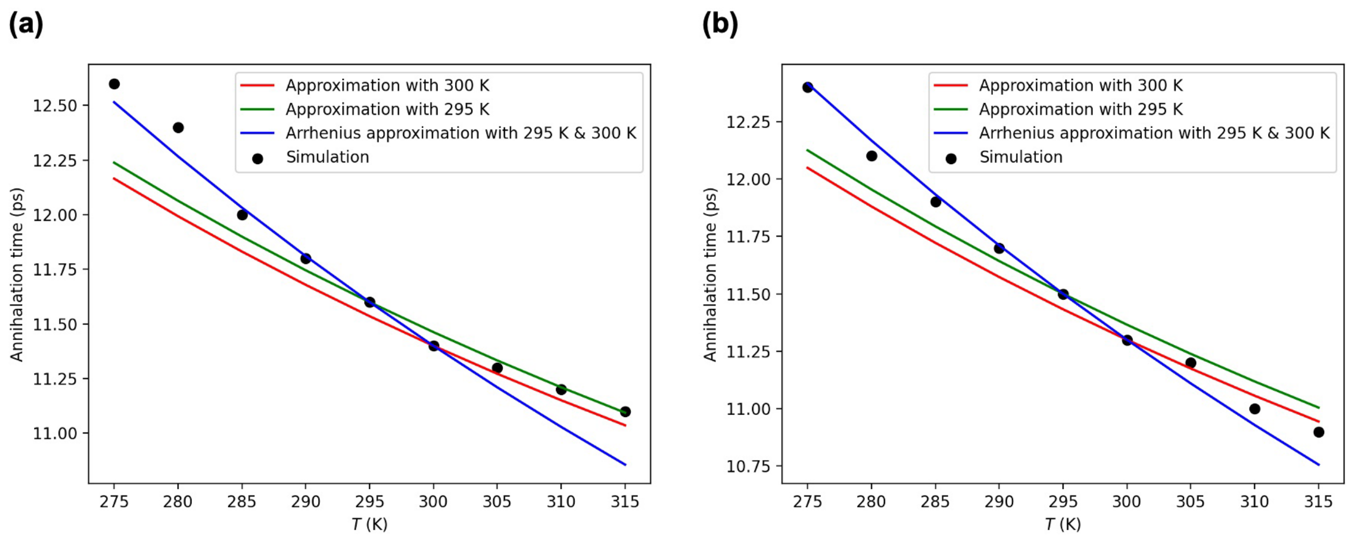

FIG. 4. Parameters are set to $A = 15$ pJ m^{-1}, $D = 3.115$ mJ m^{-2}, $K_u = 0.8$ MJ m^{-3}, and $M_s = 0.58$ MA m^{-1} for both cases. (a) Annihilation time versus temperature for $B_{ext} = 0$ T. (b) Annihilation time versus temperature for $B_{ext} = 0.005\frac{D^2}{2M_sA}$.

III. RESULTS AND DISCUSSION

A. Annihilation time

We acquire approximate formulas for the annihilation rate of skyrmioniums as in Eqs. (24) and (28):

$$J_\delta \approx \left\{ \begin{array}{l} \frac{\alpha\mathcal{Q}}{1+\alpha^2} e^{\frac{4\pi\tilde{\kappa}\delta}{\tilde{\epsilon}}\left(1-\frac{\Lambda\mathcal{Q}\delta}{\tilde{\kappa}}\right)} \left(\frac{2\tilde{\kappa}\delta}{\tilde{\epsilon}}\right)^{\frac{1}{2}} e^{-\frac{\pi\tilde{\kappa}^2}{\tilde{\epsilon}\Lambda\mathcal{Q}}},\ \tilde{\epsilon} \ll \tilde{\kappa}\delta \\ \frac{\alpha\mathcal{Q}}{(1+\alpha^2)\ln\left(\frac{\alpha\tilde{\epsilon}\tilde{c}}{\delta\tilde{\kappa}\sqrt{1+\alpha^2}}\right)} e^{-\frac{\pi\tilde{\kappa}^2}{\tilde{\epsilon}\Lambda\mathcal{Q}}},\ \delta \ll 1,\ \tilde{\kappa}\delta \ll \tilde{\epsilon} \end{array} \right\}. \quad (31)$$

We compare the micromagnetic simulation results such as Figs. 2 and 3 with the approximate annihilation time $\frac{\tau_0}{J_\delta}$ under a series of parameters. We first calibrate the Λ and confirm that it is reasonable by checking the corresponding cutoff length. Then we vary the temperature and compare our results with micromagnetic simulation results. Our approximation has described not only the dominated exponential dependence but also the deviation from variation of annihilation rate prefactor. Therefore, our approximation decays slower with increasing temperature and is closer to the simulation results than the simple Arrhenius approximation in the temperature regime higher than the calibration temperature as in Figs. 4(a) and 4(b).

Here we can also draw a phase diagram (Fig. 5) with respect to B_{ext} and T in a small regime where the change for parameters is negligible. The general trend is that the annihilation time increases with respect to B_{ext} and decreases with respect to temperature. While the temperature dependence of the annihilation time is explicitly due to the intensity of thermal noise, its relation to B_{ext} results from both the dynamical effects of B_{ext} and the change of initial size of the skyrmionium. We have simulated the initial magnetization profile under different B_{ext}. The simulations are shown in Fig. 6, which agrees with the results in Ref. [36]. The size of the skyrmionium gradually increases with respect to B_{ext}. When B_{ext} is negative enough, the skyrmionium will annihilate into a skyrmion that follows the same size relation to B_{ext} in the absence of thermal noise. We have also simulated cases where B_{ext} makes $\mathcal{Q}$ turn negative. The result is not considered because, under this set of parameters, the skyrmioniums cannot stabilize and will annihilate into skyrmions in the absence of thermal noise.

We have also simulated some negative B_{ext} cases where $|B_{ext}|$ is large, where the results deviate from our approximation. This may come from the decoupling of two skyrmions consisting the skyrmionium when the coupling is suppressed by B_{ext}. In contrast, in our preliminary approximation, we allow them to decouple only to a very limited level. As is observed in some cases in Fig. 7, the outer circular domain wall is even "penetrated," and the annihilation happens through the outer skyrmion. The outer circular domain wall develops thin enough at some position and continuity breaks down there. Hence, theoretically, under some smaller negative B_{ext}, there should exist a case where continuity breaks down at both the inner skyrmion and the outer circular domain

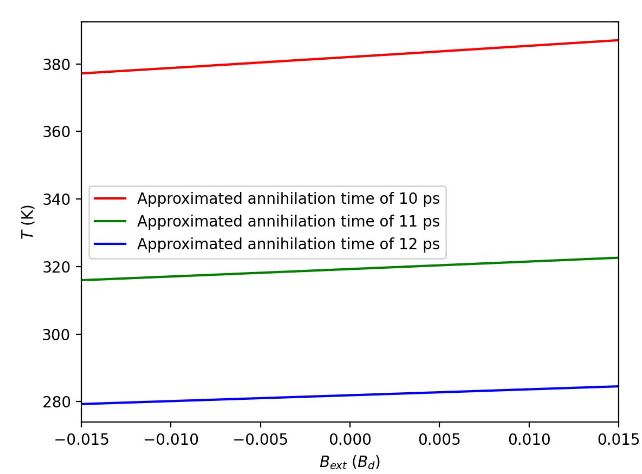

FIG. 5. Annihilation time versus perpendicular magnetic field and temperature for $A = 15$ pJ m^{-1}, $D = 3.115$ mJ m^{-2}, $K_u = 0.8$ MJ m^{-3}, $M_s = 0.58$ MA m^{-1}, and $B_d = \frac{D^2}{2M_sA}$.

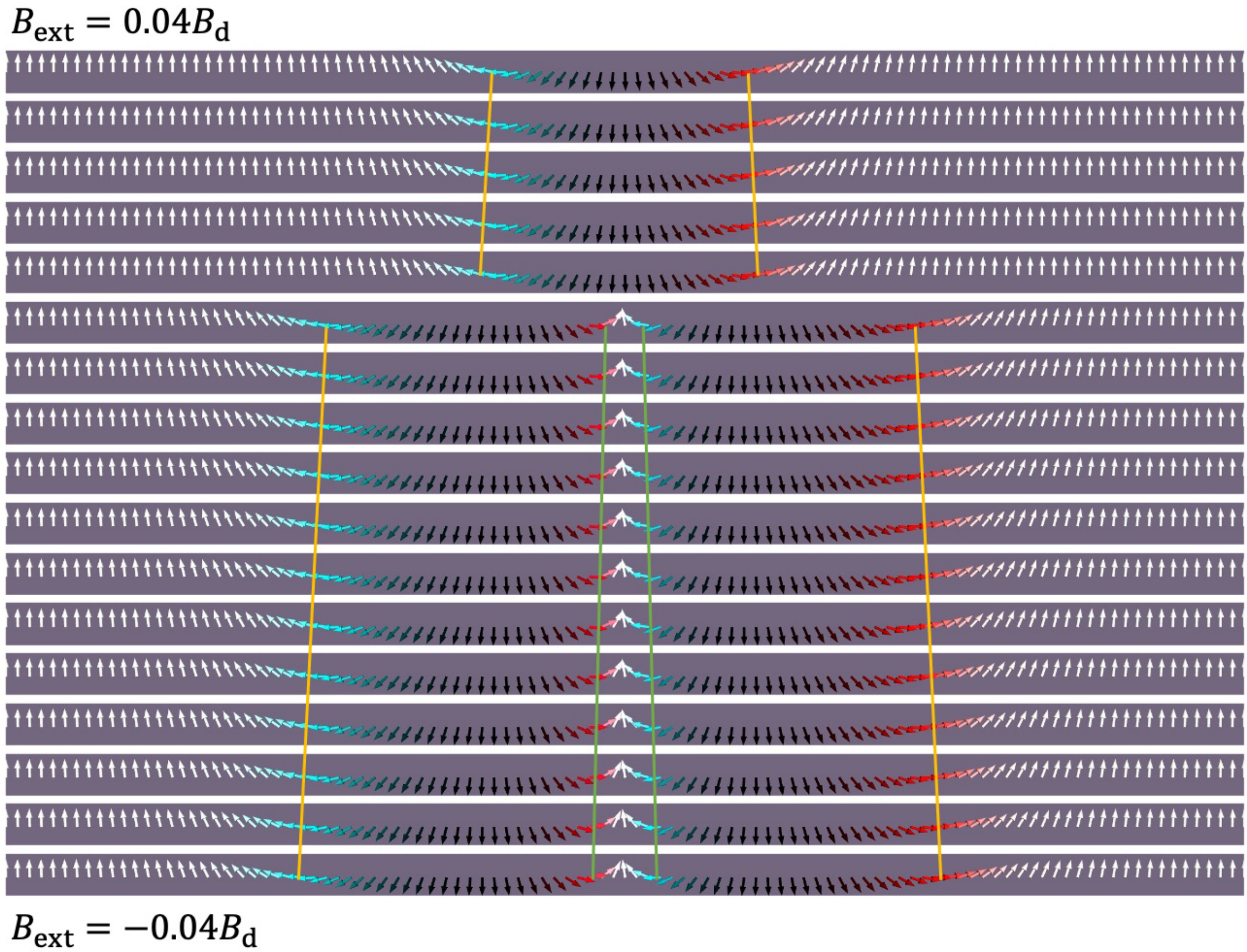

FIG. 6. Magnetization profile side view for $A = 15$ pJ m^{-1}, $D = 3.115$ mJ m^{-2}, $K_u = 0.8$ MJ m^{-3}, and $M_s = 0.58$ MA m^{-1}. Figures are colored with respect to the standard HSL color space. The length scale remains identical within the same figure. The B_{ext} values from bottom to top are $B_{\text{ext}} = -0.04B_d$ to $B_{\text{ext}} = 0.04B_d$ with an interval of $0.005B_d$, where $B_d = \frac{D^2}{2M_sA}$. The skyrmioniums and skyrmions are generated by an initial profile of $\boldsymbol{m}_z = -1$ where the radius with respect to the center of the simulation space 40 nm $> r_{\text{sim}} >$ 20 nm, $\boldsymbol{m}_z = 1$ for the rest part. The size of the skyrmionium gradually increases with respect to B_{ext}. Yellow and green lines highlight the size differences.

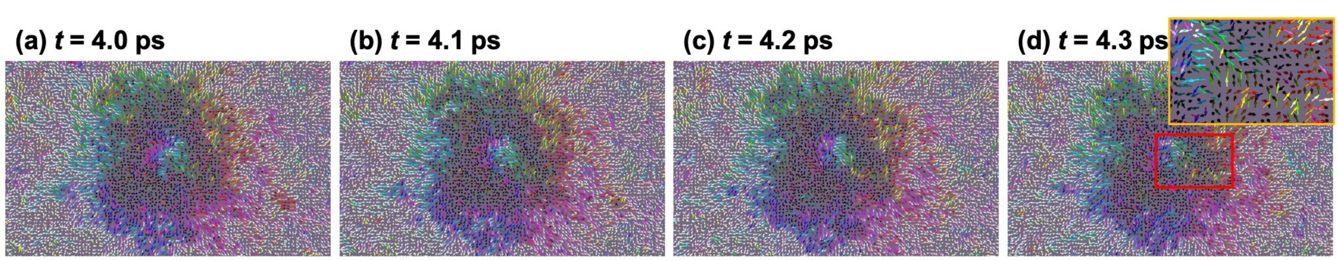

FIG. 7. Magnetization profile for $A = 15$ pJ m^{-1}, $D = 3.115$ mJ m^{-2}, $K_u = 0.8$ MJ m^{-3}, $M_s = 0.58$ MA m^{-1}, $B_{\text{ext}} = -0.03\frac{D^2}{2M_sA}$, and $T = 300$ K. Figures are colored with respect to the standard HSL color space. The length scale remains identical within the same figure. The times from panels (a) to (d) are $t = 4.0$, 4.1, 4.2, and 4.3 ps. Here the Dormand-Prince solver is used to better describe the larger magnetization dynamics due to the inhibitated coupling. The red square highlights the inner skyrmion and the "penetrating pathway." The magnified view of the area in the square is given at the top right corner. Note that here the inner skyrmion has not been annihilated yet.

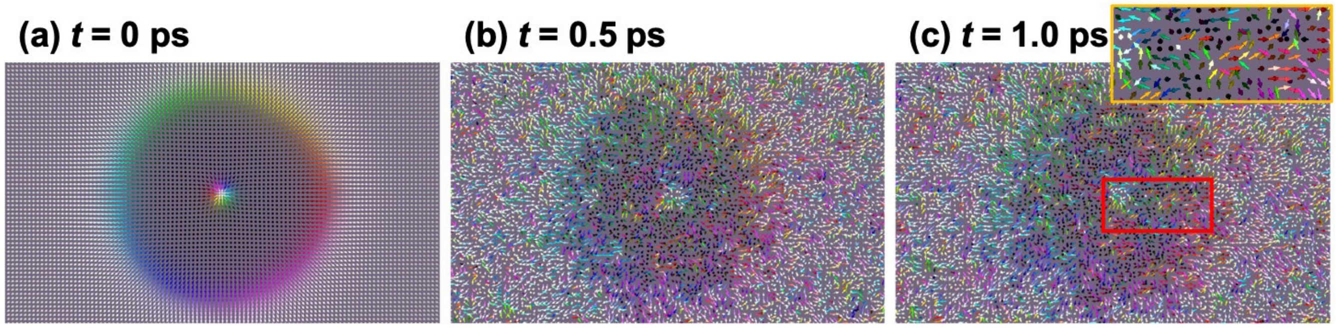

FIG. 8. Magnetization profile for $A = 15$ pJ m^{-1}, $D = 3.115$ mJ m^{-2}, $K_u = 0.8$ MJ m^{-3}, $M_s = 0.58$ MA m^{-1}, $B_{ext} = 0$ T, and $T = 500$ K. Figures are colored with respect to the standard HSL color space. The length scale remains identical within the same figure. The times from panels (a) to (c) are $t = 0.0$, 0.5, and 1.0 ps. Note that the Dormand-Prince solver is used in the simulation here for a better description of the magnetization dynamics with a relatively large change of magnetization, where the coupling between the inner and outer skyrmions is reduced. The red square highlights the inner skyrmion and the penetrating pathway. The magnified view of the area in the square is given at the top right corner. Note that here the inner skyrmion has not been annihilated yet.

wall. Further research studies could be done to investigate the detailed process of these annihilations with more freedom of decoupling.

We have also conducted simulations in the high-temperature regime; the results under this set of parameters also deviate from our approximation. This may be because of the same reason as in the large negative B_{ext} cases, for similar "penetration" events are observed as in Fig. 8. Possibly it is the thermal noise that suppresses the coupling of two skyrmions consisting the skyrmionium.

To confirm the outcome of the transition, we extend our micromagnetic simulations with a relaxation process following the previous results after the annihilation as in Fig. 9. During the annihilation, as shown in Fig. 10, the moving time average of topological charge Q_{top} in a 1-ps time window drops from 0 to -1, the energy varies from one local minima to another, which is clearer after the relaxation process. Note that there are still some fluctuations of Q_{top} from the rippling of magnetization states on the boundary edge under thermal noise, which is also reported by Kim and Mulkers [90]. Therefore, the specific annihilation time is vague under the thermal noise. Moreover, the evolution time after "capture by absorber," which also varies depending on temperature, is neglected in this preliminary approximation. Further efforts could be made towards the integration of this process and a more precise measurement of annihilation time.

B. Annihilation path

We acquired the approximate path of skyrmionium annihilation in the small noise regime when $\delta \ll 1$:

$$\tilde{z}_{opt} \approx \tilde{z}_0 \left\{ 1 - \exp\left[\frac{\alpha - i}{1 + \alpha^2} \mathcal{Q}(t - T) \right] \right\}, \qquad (32)$$

which is a spirally evolving curve on the complex plane for $\alpha \ll 1$. Consequently, when $\alpha \ll 1$, the structure rotates during the annihilation, which is similar to the annihilation process of the skyrmion [8].

It is important to note that, in principle, the outcomes obtained from the GNEB method should align with simulation results.

IV. CONCLUSION

In conclusion, by considering the topological change from the perspective of capture by absorber at microscale, we use the stochastic Landau-Lifshitz-Gilbert equation in the continuum micromagnetic framework to derive formulas describing a type of the annihilation of skyrmioniums: the thermal anni-

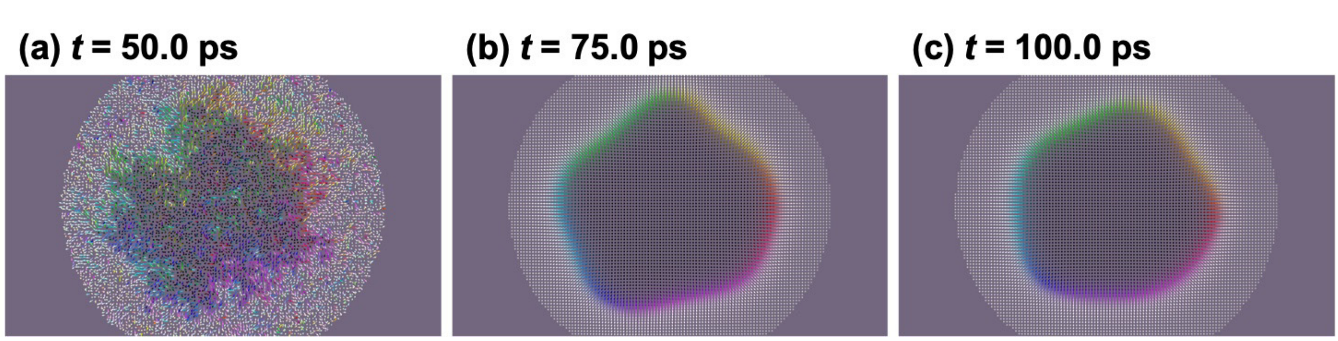

FIG. 9. Relaxation. Magnetization profile for $A = 15$ pJ m^{-1}, $D = 3.115$ mJ m^{-2}, $K_u = 0.8$ MJ m^{-3}, $M_s = 0.58$ MA m^{-1}, $B_{ext} = 0$ T, and $T = 0$ K. Figures are colored with respect to the standard HSL color space. The length scale remains identical within the same figure. The times from panels (a) to (c) are $t = 50.0$, 75.0, and 100.0 ps. The structure is gradually stabilized and appears as a skyrmion, which is confirmed by topological charge calculation.

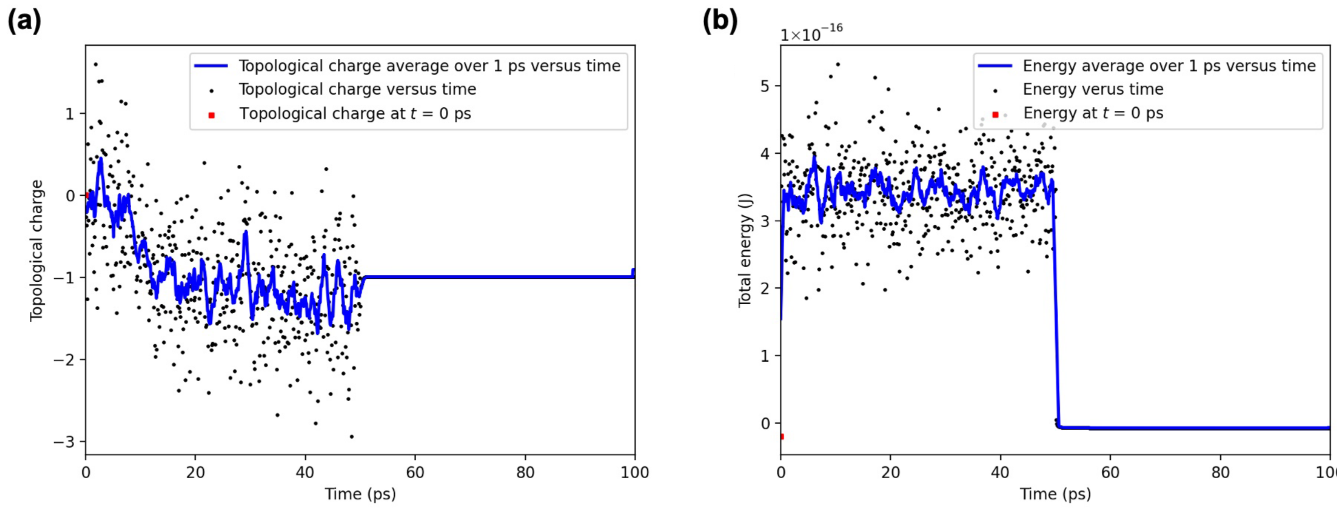

FIG. 10. (a) Topological charge versus time. (b) Energy versus time. Parameters: $A = 15$ pJ m^{-1}, $D = 3.115$ mJ m^{-2}, $K_\mathrm{u} = 0.8$ MJ m^{-3}, $M_\mathrm{s} = 0.58$ MA m^{-1}, and $B_\mathrm{ext} = 0$ T. The temperature is $T = 300$ K when $t < 50$ ps and $T = 0$ K when $t > 50$ ps. The boundary is accentuated with $K_\mathrm{u} = 8$ MJ m^{-3} where the radius with respect to the center of the simulation space $r_\mathrm{sim} > 60$ nm. The magnetization profiles away from the boundary as in Figs. 2, 3, and 9 comply with data in the plots with respect to time. Note that here we average the data at the center of the averaging period, which may experience underfitting and requires extra direct observation over the 0.5-ps period at both ends. The initial value for the topological charge is 0 and the initial value for the total energy is slightly lower than 0.

hilation of the skyrmion inside the skyrmionium that leads to the transformation of the skyrmionium into a skyrmion. The derived formulas provide reasonably good approximations of the skyrmionium collapse rate involving the variation of prefactor and collapse path, with only low computational cost and few microscopic details required. Future atomistic approach research studies could help to obtain further details and consequentially help to improve the analytical models. Our results could further improve the manipulation of skyrmioniums and provide guidance in the prospective applications of skyrmioniums in spintronic devices.

ACKNOWLEDGMENTS

A.J. and Y.Z. acknowledge support by the Shenzhen Peacock Group Plan (Grant No. KQTD20180413181702403), the National Natural Science Foundation of China (Grants No. 12374123), the Guangdong Basic and Applied Basic Research Foundation (Grant No. 2021B1515120047), the Shenzhen Fundamental Research Fund (Grant No. JCYJ20210324120213037), and the SZSTI stable support scheme. X.Z. and M.M. acknowledge support by CREST, the Japan Science and Technology Agency (Grant No. JPMJCR20T1). M.M. also acknowledges support by the Grants-in-Aid for Scientific Research from JSPS KAKENHI (Grants No. JP23H04522 and No. JP20H00337) and the Waseda University Grant for Special Research Projects (Grant No. 2023C-140).

APPENDIX A: SIMULATION METHODS

The simulations are performed by using the open-source micromagnetic simulator MUMAX3 [84]. Parameters have been extracted from the simulation results for calibration purposes. These parameters are then processed using custom-written PYTHON codes to derive the approximate analytical results, which are subsequently compared with the simulation outcomes.

Considering the arbitrariness of thermal noise, here we use the Bogaki-Shampine method for better stability and to be consistent with the static calculations [85]. Here we choose $A = 15$ pJ m^{-1}, $M_\mathrm{s} = 0.58$ MA m^{-1}, $K_\mathrm{u} = 0.8$ MJ m^{-3}, $d = 0.4$ nm, and $\alpha = 0.3$, which yields $l_\mathrm{ex} = 8.4$ nm and $\tau_0 = 7.8$ ps [91]. The simulation space is a cylinder with a diameter of $320d$ and a height of d, and the cell size is (d, d, d).

Here we recorded the annihilation time by looking at the magnetization profile at the core and confirmed the annihilation by checking the topological charge after a relaxation process, which is defined as $Q_\mathrm{top} = (4\pi)^{-1} \int_{\mathbb{R}^2} \boldsymbol{m} \cdot (\boldsymbol{m}_x \times \boldsymbol{m}_y) dS$, where $\boldsymbol{m}_x$ and $\boldsymbol{m}_y$ are partial derivatives of $\boldsymbol{m}$ with respect to x and y. As is suggested by Kim and Mulkers [90], using the function ext_topologicalchargelattice in MUMAX3, we follow the approach of Berg and Lüscher [92] to mitigate the fluctuation of topological charge originated from inaccuracies of the finite-difference approximations of Q_top when large spatial variations of $\boldsymbol{m}$ occur under thermal noises. To prevent the unstable local magnetization reversals on the boundary edge under thermal noise from causing the total topological charge to deviate, we introduce a reinforced perpendicular anisotropy condition limited on the boundary edge when calculating the topological charge. We confirmed that the magnetization at the core is almost identical no matter whether the strengthening boundary condition is applied or not with figures like Fig. 11. Hence, topological charge calculated with the accentuated boundary condition, like in Fig. 10, is credible for investigating the change of the core.

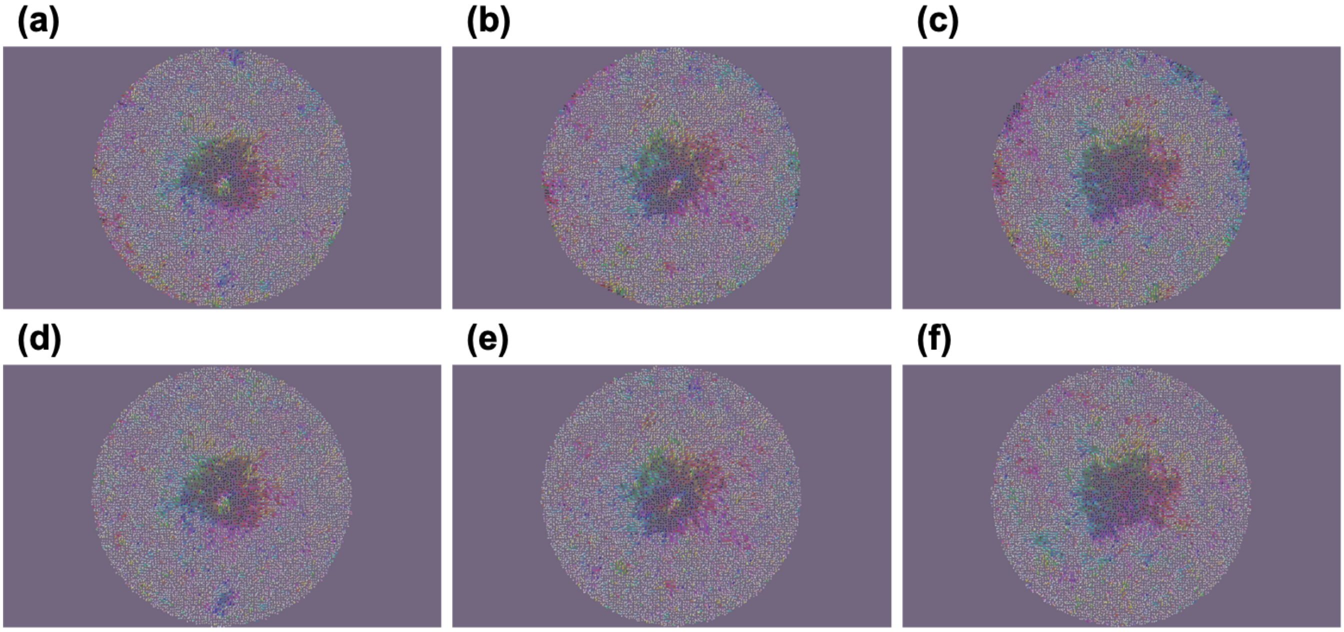

FIG. 11. Magnetization profile with $A = 15$ pJ m^{-1}, $D = 3.115$ mJ m^{-2}, $K_u = 0.8$ MJ m^{-3}, $M_s = 0.58$ MA m^{-1}, $B_{ext} = 0$ T, and $T = 300$ K. Figures are colored with respect to the HSL color space. The length scale remains identical within the same figure. The times are $t = 5.0$, 10.0, and 15.0 ps for panels (a) to (c) and panels (d) to (f). For panels (d), (e), and (f), the boundary is accentuated with $K_u = 8$ MJ m^{-3} where the radius with respect to the center of the simulation space $r_{sim} > 60$ nm. The magnetization profile at the core remains identical.

APPENDIX B: SKYRMIONIUM PROFILE

1. Energy verification

We consider the center of the skyrmionium to be $\boldsymbol{r}_0(t)$, and we introduce the polar coordinates $[\boldsymbol{r}, \psi]$ to be $\boldsymbol{r} = \boldsymbol{r}_0 + [r\cos(\psi), r\sin(\psi)]$.

As is mentioned in the main text, we propose a reduced core profile of skyrmioniums as follows:

$$\begin{aligned}\theta(r) &\simeq \theta_{Sk}\left(-\frac{r}{\delta_{Sk}} + R_{Sk}\right) + \theta_{Sk}\left(-\frac{r}{\delta_{Sk}} - R_{Sk}\right)\\ &\simeq 2\arctan\left(\frac{-\frac{r}{\delta_{Sk}} + R_{Sk}}{\rho_{Sk}}\right) + 2\arctan\left(\frac{-\frac{r}{\delta_{Sk}} - R_{Sk}}{\rho_{Sk}}\right).\end{aligned} \tag{B1}$$

Without loss of generality, we can set $\rho_{Sk} = 1$ and vary the parameters δ_{Sk} and R_{Sk} to get all possible profiles. We define $\mathcal{A} = \frac{\delta_{Sk}(1+R_{Sk}^2)}{2}$ and $\mathcal{B} = \frac{1}{2\delta_{Sk}}$, and the core profile becomes

$$\begin{aligned}\theta(r) &\simeq \theta_{Sk}\left(-\frac{r}{\delta_{Sk}} + R_{Sk}\right) + \theta_{Sk}\left(-\frac{r}{\delta_{Sk}} - R_{Sk}\right)\\ &\simeq 2\arctan\left(\frac{r}{\mathcal{A} - \mathcal{B}r^2}\right) + 2\pi n,\end{aligned} \tag{B2}$$

where $n \in \mathbb{Z}$ are some integers that make the curve smooth.

The profile at the tail is approximately

$$[2\pi - \theta(r)] \propto K_1\left(\frac{r}{\mathcal{L}_s}\right), \tag{B3}$$

where $K_1(z)$ is the modified Bessel function of the second kind, which is approximately $K_1(\frac{r}{\mathcal{L}_s}) \approx e^{-\frac{r}{\mathcal{L}_s}} r^{-\frac{1}{2}}$.

Both at the core and at the tail, we have

$$\phi(\boldsymbol{r}, t) = \arg[\boldsymbol{r} - \boldsymbol{r}_0(t)] + \varphi(t) - \pi, \tag{B4}$$

where $\varphi(t)$ is some fixed angle with respect to the structure, which can be interpreted as the rotation angle of the skyrmionium here.

Then we calculate the energy and compare it with that by MUMAX3 with the Bogacki-Shampine method to check the accuracy of our approximation [84,85]. We first use the radius where $\theta = \pi$, which is calculated to be $r_\pi = \sqrt{\frac{\mathcal{A}}{\mathcal{B}}}$, to calibrate the parameters. By calculating the energy of different parameters and identifying the energy minima under the contraint of r_π, we find δ_{Sk} and R_{Sk}. Here we use the core profile to as far as $2r_\pi$ to better characterize the skyrmioniums, and we choose a suitable tail profile for the rest area so the profile remains continuous. As shown from Figs. 12–16, we varied the parameters and confirmed that the energy difference is within 26% in the selected parameter space.

2. Integrals

From the core profile, we have

$$\sin\theta = \frac{2(\mathcal{A} - \mathcal{B}r^2)r}{r^2 + (\mathcal{A} - \mathcal{B}r^2)^2}, \tag{B5}$$

$$\cos\theta = \frac{(\mathcal{A} - \mathcal{B}r^2)^2 - r^2}{r^2 + (\mathcal{A} - \mathcal{B}r^2)^2}. \tag{B6}$$

Since we are considering the core profile, the equations approximately are

$$\sin\theta \approx \frac{2\mathcal{A}r}{\mathcal{A}^2 + (1 - 2\mathcal{A}\mathcal{B})r^2}, \tag{B7}$$

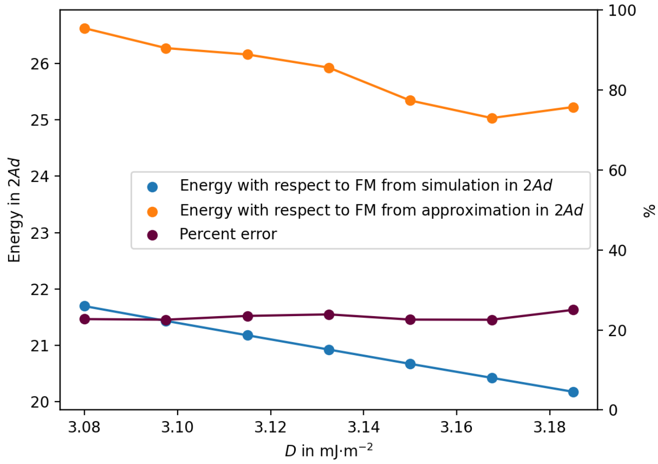

FIG. 12. Energy versus DMI coefficient with $A = 15$ pJ m^{-1}, $K_\mathrm{u} = 0.8$ MJ m^{-3}, $M_\mathrm{s} = 0.58$ MA m^{-1}, and $B_\mathrm{ext} = 0$ T.

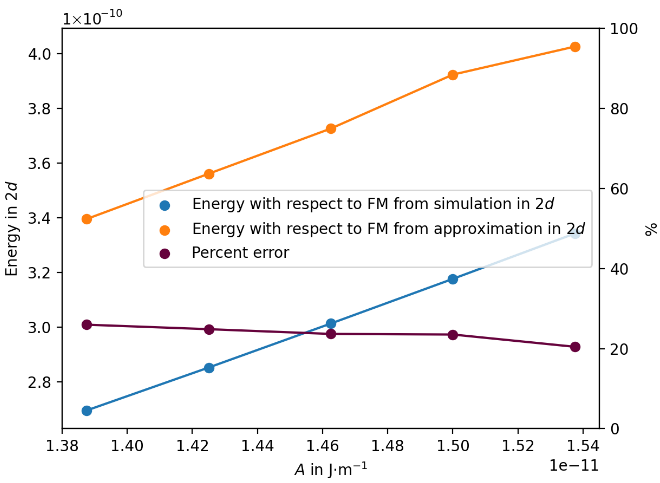

FIG. 13. Energy versus exchange coefficient with $D = 3.115$ mJ m^{-2}, $K_\mathrm{u} = 0.8$ MJ m^{-3}, $M_\mathrm{s} = 0.58$ MA m^{-1}, and $B_\mathrm{ext} = 0$ T.

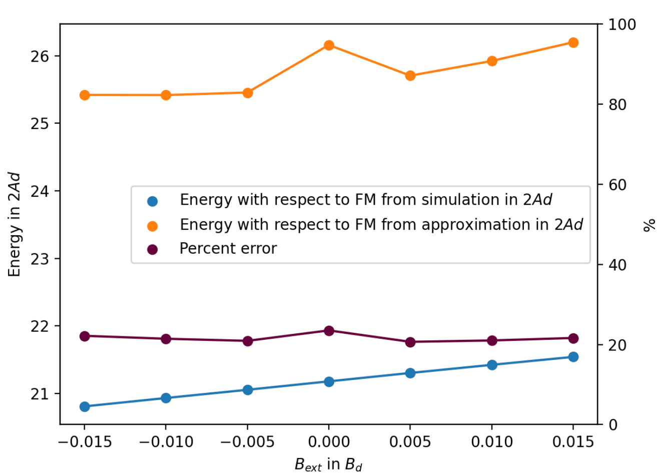

FIG. 14. Energy versus perpendicular magnetic field strength with $A = 15$ pJ m^{-1}, $D = 3.115$ mJ m^{-2}, $K_\mathrm{u} = 0.8$ MJ m^{-3}, and $M_\mathrm{s} = 0.58$ MA m^{-1}. $B_\mathrm{d} = \frac{D^2}{2M_\mathrm{s}A}$ is defined for simplicity.

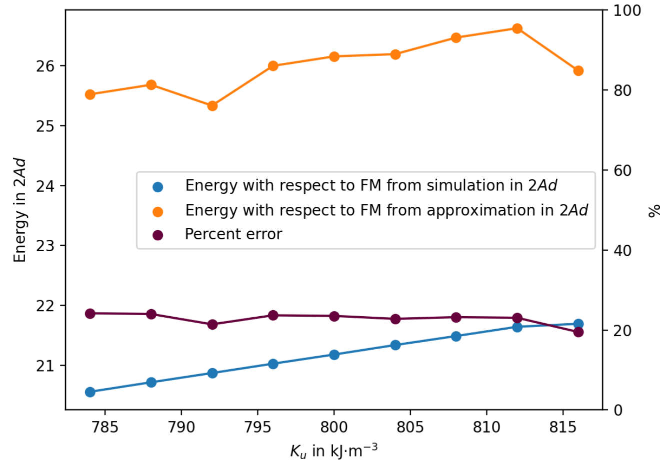

FIG. 15. Energy versus anisotropy coefficient with $A = 15$ pJ m^{-1}, $D = 3.115$ mJ m^{-2}, $M_\mathrm{s} = 0.58$ MA m^{-1}, and $B_\mathrm{ext} = 0$ T.

$$\cos\theta \approx \frac{\mathcal{A}^2 - (1 + 2\mathcal{A}\mathcal{B})r^2}{\mathcal{A}^2 + (1 - 2\mathcal{A}\mathcal{B})r^2}. \tag{B8}$$

Similarly, we have

$$\theta_r = \frac{2\mathcal{A} + 2\mathcal{B}r^2}{\mathcal{A}^2 + (1 - 2\mathcal{A}\mathcal{B})r^2} \approx \frac{2\mathcal{A}}{\mathcal{A}^2 + (1 - 2\mathcal{A}\mathcal{B})r^2}, \tag{B9}$$

$$\begin{aligned}\theta_t &= -\theta_r \dot{\boldsymbol{r}}_0(\cos\psi, \sin\psi) - \frac{2r\frac{\partial(\mathcal{A} - \mathcal{B}r^2)}{\partial t}}{\mathcal{A}^2 + (1 - 2\mathcal{A}\mathcal{B})r^2} \\ &\approx -\theta_r \dot{\boldsymbol{r}}_0(\cos\psi, \sin\psi) - \frac{2\dot{\mathcal{A}}r}{\mathcal{A}^2 + (1 - 2\mathcal{A}\mathcal{B})r^2},\end{aligned} \tag{B10}$$

$$\phi_t = \frac{\dot{\boldsymbol{r}}_0}{r}(\sin\psi, -\cos\psi) + \dot{\varphi}, \tag{B11}$$

$$\theta_x = \theta_r \cos\psi, \;\; \theta_y = \theta_r \sin\psi, \tag{B12}$$

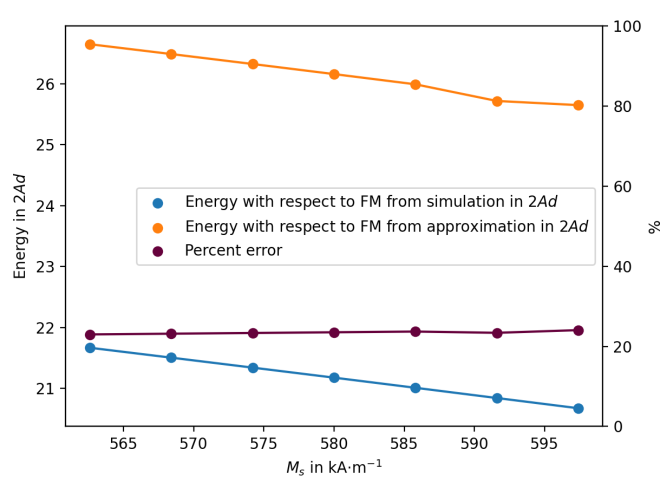

FIG. 16. Energy versus saturation magnetization with $A = 15$ pJ m^{-1}, $D = 3.115$ mJ m^{-2}, $K_\mathrm{u} = 0.8$ MJ m^{-3}, and $B_\mathrm{ext} = 0$ T.

$$\phi_x = -\frac{\sin\psi}{r},\ \phi_y = \frac{\cos\psi}{r}. \tag{B13}$$

Then we calculate the integrals, with the cutoff length $\mathcal{L}$ introduced when logarithmic divergence is presented; hence, the formula is valid even if the outer solution does not have adequate relaxation time. Also, we introduce $\mathcal{C}^2 = \frac{\mathcal{A}^2}{1-2\mathcal{A}\mathcal{B}}$ and $\mathcal{D} = \frac{\mathcal{A}}{1-2\mathcal{A}\mathcal{B}}$, which yields

$$\int_{\mathbb{R}^2} \sin^2(\theta)dS \approx 8\pi\mathcal{D}^2 \int_0^{\frac{\mathcal{L}}{\mathcal{C}}} \frac{z^3}{(1+z^2)^2}dz \approx 8\pi\mathcal{D}^2\ln\left(\frac{\mathcal{L}}{\mathcal{C}}\right), \tag{B14}$$

$$\int_{\mathbb{R}^2} r\theta_r\frac{\sin(2\theta)}{2}dS \approx \int_0^{\frac{\mathcal{L}}{\mathcal{C}}} 8\pi\mathcal{D}^2z^3\frac{\mathcal{C}^2-(2\mathcal{D}^2-\mathcal{C}^2)z^2}{\mathcal{C}^2(1+z^2)^3}dz \approx 8\pi\mathcal{D}^2\frac{\mathcal{C}^2-2\mathcal{D}^2}{\mathcal{C}^2}\ln\left(\frac{\mathcal{L}}{\mathcal{C}}\right), \tag{B15}$$

$$\int_{\mathbb{R}^2} (r\theta_r)^2dS \approx 8\pi\mathcal{D}^2 \int_0^{\frac{\mathcal{L}}{\mathcal{C}}} \frac{z^3}{(1+z^2)^2}dz \approx 8\pi\mathcal{D}^2\ln\left(\frac{\mathcal{L}}{\mathcal{C}}\right), \tag{B16}$$

$$\int_{\mathbb{R}^2} \theta_r\sin^2(\theta)dS \approx \frac{16\pi\mathcal{D}^3}{\mathcal{C}^2}\int_0^{\frac{\mathcal{L}}{\mathcal{C}}} \frac{z^3}{(1+z^2)^3}dz \approx \frac{4\pi\mathcal{D}^3}{\mathcal{C}^2}, \tag{B17}$$

$$\int_{\mathbb{R}^2} r\theta_r\theta_t dS \approx \frac{\dot{\mathcal{A}}}{\mathcal{A}}\int_0^{\frac{\mathcal{L}}{\mathcal{C}}} \frac{-8\pi\mathcal{D}^2z^3}{(1+z^2)^2}dz \approx -8\pi\mathcal{D}^2\frac{\dot{\mathcal{A}}}{\mathcal{A}}\ln\left(\frac{\mathcal{L}}{\mathcal{C}}\right). \tag{B18}$$

Note that the equations only apply to $\mathcal{D} > 0$ cases and cases with $\mathcal{L}$ limited so some integrals remain convergent.

APPENDIX C: REDUCTION INTO FINITE-DIMENSIONAL SYSTEM

We substitute the skyrmionium profile into the integral identities, which approximately yields

$$\frac{d}{dt}\begin{bmatrix}\ln(\mathcal{A})\\ \varphi\end{bmatrix} = -\frac{1}{1+\alpha^2}\begin{bmatrix}-1 & \alpha\\ \alpha & 1\end{bmatrix}\sqrt{\frac{\alpha\epsilon}{4\pi\mathcal{D}^2\ln\left(\frac{\mathcal{L}}{\mathcal{C}}\right)}}\begin{bmatrix}\dot{W}_1\\ \dot{W}_2\end{bmatrix} - \frac{1}{1+\alpha^2}\begin{bmatrix}-1 & \alpha\\ \alpha & 1\end{bmatrix}\begin{bmatrix}\frac{\mathcal{D}\kappa\sin\varphi}{2\mathcal{C}^2\ln\left(\frac{\mathcal{L}}{\mathcal{C}}\right)}\\ \left|\frac{1+2\mathcal{A}\mathcal{B}}{1-2\mathcal{A}\mathcal{B}}\right|(Q-1)-\frac{B_{\text{ext}}}{\mu_0M_s}-\frac{\mathcal{D}\kappa\cos\varphi}{2\mathcal{C}^2\ln\left(\frac{\mathcal{L}}{\mathcal{C}}\right)}\end{bmatrix}, \tag{C1}$$

$$\frac{d}{dt}\begin{bmatrix}x_0\\ y_0\end{bmatrix} = -\frac{1}{1+\alpha^2}\begin{bmatrix}-1 & \alpha\\ \alpha & 1\end{bmatrix}\sqrt{\frac{\alpha\epsilon\mathcal{C}^2}{2\pi\mathcal{D}^2}}\begin{bmatrix}\dot{W}_3\\ \dot{W}_4\end{bmatrix}, \tag{C2}$$

where $\boldsymbol{r}_0 = [x_0, y_0]$.

We then check the orthogonality of the Wiener processes by computing the correlators. For instance, for the first two Wiener processes, we have

$$\begin{aligned}\langle\dot{W}_1(t)\dot{W}_2(t')\rangle &= \frac{1}{\mathcal{A}_{W_1}\mathcal{B}_{W_1}}\int_{\mathbb{R}^2}\int_{\mathbb{R}^2}\langle\sin[\theta(\boldsymbol{r},t)]\zeta(\boldsymbol{r},t)\{\boldsymbol{r}'\cdot\nabla[\theta(\boldsymbol{r}',t')]\eta(\boldsymbol{r}',t')+\sin[\theta(\boldsymbol{r}',t')]\boldsymbol{r}'\cdot\nabla[\phi(\boldsymbol{r}',t')]\zeta(\boldsymbol{r}',t')\}\rangle d^2rd^2r'\\ &= \frac{\delta(t-t')}{\mathcal{A}_{W_1}\mathcal{B}_{W_1}}\int_{\mathbb{R}^2}\sin^2(\theta)\boldsymbol{r}\cdot\nabla\phi d^2r \simeq 0,\end{aligned} \tag{C3}$$

where $\mathcal{A}_{W_1} = \sqrt{\int_{\mathbb{R}^2}\sin^2(\theta)dS}$ and $\mathcal{B}_{W_1} = \sqrt{\int_{\mathbb{R}^2}[|\nabla\theta\cdot(\boldsymbol{r}-\boldsymbol{r}_0)|^2+|\sin(\theta)\nabla\phi\cdot(\boldsymbol{r}-\boldsymbol{r}_0)|^2]dS}$. Similarly, other correlators can be checked. Then we introduce another set of mutually independent Wiener processes for simplicity:

$$\tilde{W}_1 = -\frac{\alpha W_1 - W_2}{\sqrt{1+\alpha^2}},\ \tilde{W}_2 = -\frac{W_1+\alpha W_2}{\sqrt{1+\alpha^2}}, \tag{C4}$$

$$\tilde{W}_3 = -\frac{\alpha W_3 + W_4}{\sqrt{1+\alpha^2}},\ \tilde{W}_4 = -\frac{\alpha W_4 - W_3}{\sqrt{1+\alpha^2}}. \tag{C5}$$

Then Eqs. (C1) and (C2) become

$$\frac{d}{dt}\begin{bmatrix}\ln(\mathcal{A})\\ \varphi\end{bmatrix} = \sqrt{\frac{\alpha\epsilon}{4\pi\mathcal{D}^2(1+\alpha^2)\ln\left(\frac{\mathcal{L}}{\mathcal{C}}\right)}}\begin{bmatrix}\dot{\tilde{W}}_1\\ \dot{\tilde{W}}_2\end{bmatrix} - \frac{1}{1+\alpha^2}\begin{bmatrix}-1 & \alpha\\ \alpha & 1\end{bmatrix}\begin{bmatrix}\frac{\mathcal{D}\kappa\sin\varphi}{2\mathcal{C}^2\ln\left(\frac{\mathcal{L}}{\mathcal{C}}\right)}\\ \left|\frac{1+2\mathcal{A}\mathcal{B}}{1-2\mathcal{A}\mathcal{B}}\right|(Q-1)-\frac{B_{\text{ext}}}{\mu_0M_s}-\frac{\mathcal{D}\kappa\cos\varphi}{2\mathcal{C}^2\ln\left(\frac{\mathcal{L}}{\mathcal{C}}\right)}\end{bmatrix}, \tag{C6}$$

$$\frac{d}{dt}\begin{bmatrix}x_0\\ y_0\end{bmatrix} = \sqrt{\frac{\alpha\epsilon\mathcal{C}^2}{2\pi(1+\alpha^2)\mathcal{D}^2}}\begin{bmatrix}\dot{\tilde{W}}_3\\ \dot{\tilde{W}}_4\end{bmatrix}. \tag{C7}$$

[1] T. Skyrme, A unified field theory of mesons and baryons, Nucl. Phys. **31**, 556 (1962).
[2] A. Bogdanov and A. Hubert, The stability of vortex-like structures in uniaxial ferromagnets, J. Magn. Magn. Mater. **195**, 182 (1999).
[3] A. Bogdanov and D. Yablonskii, Thermodynamically stable "vortices" in magnetically ordered crystals. The mixed state of magnets, Zh. Eksp. Teor. Fiz. **95**, 178 (1989) [Sov. Phys. JETP **68**, 101 (1989)].
[4] U. K. Rößler, A. N. Bogdanov, and C. Pfleiderer, Spontaneous skyrmion ground states in magnetic metals, Nature (London) **442**, 797 (2006).
[5] X. Z. Yu, Y. Onose, N. Kanazawa, J. H. Park, J. H. Han, Y. Matsui, N. Nagaosa, and Y. Tokura, Real-space observation of a two-dimensional skyrmion crystal, Nature (London) **465**, 901 (2010).
[6] A. Monteil, C. B. Muratov, T. M. Simon, and V. V. Slastikov, Magnetic skyrmions under confinement, Commun. Math. Phys. **404**, 1571 (2023).
[7] G. D. Fratta, C. B. Muratov, and V. V. Slastikov, Reduced energies for thin ferromagnetic films with perpendicular anisotropy, arXiv:2306.07634.
[8] S. Rohart, J. Miltat, and A. Thiaville, Path to collapse for an isolated Néel skyrmion, Phys. Rev. B **93**, 214412 (2016).
[9] Y. Jibiki, M. Goto, E. Tamura, J. Cho, S. Miki, R. Ishikawa, H. Nomura, T. Srivastava, W. Lim, S. Auffret, C. Baraduc, H. Bea, and Y. Suzuki, Skyrmion Brownian circuit implemented in continuous ferromagnetic thin film, Appl. Phys. Lett. **117**, 082402 (2020).
[10] D. Cortés-Ortuño, W. Wang, M. Beg, R. A. Pepper, M.-A. Bisotti, R. Carey, M. Vousden, T. Kluyver, O. Hovorka, and H. Fangohr, Thermal stability and topological protection of skyrmions in nanotracks, Sci. Rep. **7**, 4060 (2017).
[11] R. Ishikawa, M. Goto, H. Nomura, and Y. Suzuki, Implementation of skyrmion cellular automaton using Brownian motion and magnetic dipole interaction, Appl. Phys. Lett. **119**, 072402 (2021).
[12] J. Wang, M. Strungaru, S. Ruta, A. Meo, Y. Zhou, A. Deák, L. Szunyogh, P.-I. Gavriloaea, R. Moreno, O. Chubykalo-Fesenko, J. Wu, Y. Xu, R. F. L. Evans, and R. W. Chantrell, Spontaneous creation and annihilation dynamics of magnetic skyrmions at elevated temperature, Phys. Rev. B **104**, 054420 (2021).
[13] J. Zázvorka, F. Jakobs, D. Heinze, N. Keil, S. Kromin, S. Jaiswal, K. Litzius, G. Jakob, P. Virnau, D. Pinna, K. Everschor-Sitte, L. Rózsa, A. Donges, U. Nowak, and M. Kläui, Thermal skyrmion diffusion used in a reshuffler device, Nat. Nanotechnol. **14**, 658 (2019).
[14] J. Hagemeister, N. Romming, K. von Bergmann, E. Y. Vedmedenko, and R. Wiesendanger, Stability of single skyrmionic bits, Nat. Commun. **6**, 8455 (2015).
[15] M. Mochizuki and S. Seki, Dynamical magnetoelectric phenomena of multiferroic skyrmions, J. Phys.: Condens. Matter **27**, 503001 (2015).
[16] X. Zhang, Y. Zhou, K. Mee Song, T.-E. Park, J. Xia, M. Ezawa, X. Liu, W. Zhao, G. Zhao, and S. Woo, Skyrmion-electronics: writing, deleting, reading and processing magnetic skyrmions toward spintronic applications, J. Phys.: Condens. Matter **32**, 143001 (2020).
[17] F. Jonietz, S. Mühlbauer, C. Pfleiderer, A. Neubauer, W. Münzer, A. Bauer, T. Adams, R. Georgii, P. Böni, R. A. Duine, K. Everschor, M. Garst, and A. Rosch, Spin transfer torques in MnSi at ultralow current densities, Science **330**, 1648 (2010).
[18] X. Z. Yu, N. Kanazawa, Y. Onose, K. Kimoto, W. Z. Zhang, S. Ishiwata, Y. Matsui, and Y. Tokura, Near room-temperature formation of a skyrmion crystal in thin-films of the helimagnet FeGe, Nat. Mater. **10**, 106 (2011).
[19] N. Nagaosa and Y. Tokura, Topological properties and dynamics of magnetic skyrmions, Nat. Nanotechnol. **8**, 899 (2013).
[20] K. Litzius, J. Leliaert, P. Bassirian, D. Rodrigues, S. Kromin, I. Lemesh, J. Zázvorka, K.-J. Lee, J. Mulkers, N. Kerber, D. Heinze, N. Keil, R. Reeve, M. Weigand, B. Waeyenberge, G. Schütz, K. Everschor-Sitte, G. Beach, and M. Kläui, The role of temperature and drive current in skyrmion dynamics, Nat. Electron. **3**, 30 (2020).
[21] J. Zang, M. Mostovoy, J. H. Han, and N. Nagaosa, Dynamics of skyrmion crystals in metallic thin films, Phys. Rev. Lett. **107**, 136804 (2011).
[22] K. Litzius, I. Lemesh, B. Krüger, P. Bassirian, L. Caretta, K. Richter, F. Büttner, K. Sato, O. A. Tretiakov, J. Förster, R. M. Reeve, M. Weigand, I. Bykova, H. Stoll, G. Schütz, G. S. D. Beach, and M. Kläui, Skyrmion hall effect revealed by direct time-resolved x-ray microscopy, Nat. Phys. **13**, 170 (2017).
[23] W. Jiang, X. Zhang, G. Yu, W. Zhang, X. Wang, M. Benjamin Jungfleisch, J. E. Pearson, X. Cheng, O. Heinonen, K. L. Wang, Y. Zhou, A. Hoffmann, and S. G. E. te Velthuis, Direct observation of the skyrmion Hall effect, Nat. Phys. **13**, 162 (2017).
[24] C. Reichhardt and C. J. O. Reichhardt, Noise fluctuations and drive dependence of the skyrmion Hall effect in disordered systems, New J. Phys. **18**, 095005 (2016).
[25] R. Streubel, L. Han, M.-Y. Im, F. Kronast, U. K. Rößler, F. Radu, R. Abrudan, G. Lin, O. G. Schmidt, P. Fischer, and D. Makarov, Manipulating topological states by imprinting noncollinear spin textures, Sci. Rep. **5**, 8787 (2015).
[26] J. Hagemeister, A. Siemens, L. Rózsa, E. Y. Vedmedenko, and R. Wiesendanger, Controlled creation and stability of $k\pi$ skyrmions on a discrete lattice, Phys. Rev. B **97**, 174436 (2018).
[27] M. Finazzi, M. Savoini, A. R. Khorsand, A. Tsukamoto, A. Itoh, L. Duò, A. Kirilyuk, T. Rasing, and M. Ezawa, Laser-induced magnetic nanostructures with tunable topological properties, Phys. Rev. Lett. **110**, 177205 (2013).
[28] F. Zheng, H. Li, S. Wang, D. Song, C. Jin, W. Wei, A. Kovács, J. Zang, M. Tian, Y. Zhang, H. Du, and R. E. Dunin-Borkowski, Direct imaging of a zero-field target skyrmion and its polarity switch in a chiral magnetic nanodisk, Phys. Rev. Lett. **119**, 197205 (2017).
[29] S. Zhang, F. Kronast, G. van der Laan, and T. Hesjedal, Real-space observation of skyrmionium in a ferromagnet-magnetic topological insulator heterostructure, Nano Lett. **18**, 1057 (2018).
[30] Y. Zhang, C. Xu, P. Chen, Y. Nahas, S. Prokhorenko, and L. Bellaiche, Emergence of skyrmionium in a two-dimensional $CrGe(Se, Te)_3$ Janus monolayer, Phys. Rev. B **102**, 241107(R) (2020).
[31] N. Kent, R. Streubel, C.-H. Lambert, A. Ceballos, S.-G. Je, S. Dhuey, M.-Y. Im, F. Büttner, F. Hellman, S. Salahuddin, and P. Fischer, Generation and stability of structurally imprinted target skyrmions in magnetic multilayers, Appl. Phys. Lett. **115**, 112404 (2019).

[32] L. Bo, R. Zhao, C. Hu, Z. Shi, W. Chen, X. Zhang, and M. Yan, Formation of skyrmion and skyrmionium in confined nanodisk with perpendicular magnetic anisotropy, J. Phys. D **53**, 195001 (2020).

[33] H. Vigo-Cotrina and A. Guimarães, Creating skyrmions and skyrmioniums using oscillating perpendicular magnetic fields, J. Magn. Magn. Mater. **507**, 166848 (2020).

[34] J. Tang, Y. Wu, W. Wang, L. Kong, B. Lv, W. Wei, J. Zang, M. Tian, and H. Du, Magnetic skyrmion bundles and their current-driven dynamics, Nat. Nanotechnol. **16**, 1086 (2021).

[35] R. Msiska, D. R. Rodrigues, J. Leliaert, and K. Everschor-Sitte, Nonzero skyrmion Hall effect in topologically trivial structures, Phys. Rev. Appl. **17**, 064015 (2022).

[36] X. Zhang, J. Xia, Y. Zhou, D. Wang, X. Liu, W. Zhao, and M. Ezawa, Control and manipulation of a magnetic skyrmionium in nanostructures, Phys. Rev. B **94**, 094420 (2016).

[37] A. G. Kolesnikov, M. E. Stebliy, A. S. Samardak, and A. V. Ognev, Skyrmionium–high velocity without the skyrmion Hall effect, Sci. Rep. **8**, 16966 (2018).

[38] B. Göbel, A. F. Schäffer, J. Berakdar, I. Mertig, and S. S. P. Parkin, Electrical writing, deleting, reading, and moving of magnetic skyrmioniums in a racetrack device, Sci. Rep. **9**, 12119 (2019).

[39] S. Li, J. Xia, X. Zhang, M. Ezawa, W. Kang, X. Liu, Y. Zhou, and W. Zhao, Dynamics of a magnetic skyrmionium driven by spin waves, Appl. Phys. Lett. **112**, 142404 (2018).

[40] B. Göbel, I. Mertig, and O. A. Tretiakov, Beyond skyrmions: Review and perspectives of alternative magnetic quasiparticles, Phys. Rep. **895**, 1 (2021).

[41] J. Zhang, M. Xu, Z. Zhang, G. Jiang, and D. Meng, Generation and steady motion of skyrmionium in racetracks under successive pulsed currents and magnetic fields, Phys. Lett. A **451**, 128433 (2022).

[42] X. Liang, X. Zhang, L. Shen, J. Xia, M. Ezawa, X. Liu, and Y. Zhou, Dynamics of ferrimagnetic skyrmionium driven by spin-orbit torque, Phys. Rev. B **104**, 174421 (2021).

[43] S. Yang, Y. Zhao, K. Wu, Z. Chu, X. Xu, X. Li, J. Akerman, and Y. Zhou, Reversible conversion between skyrmions and skyrmioniums, Nat. Commun. **14**, 3406 (2023).

[44] Z. Zhang, M. Xu, G. Jiang, J. Zhang, D. Meng, W. Chen, Y. Chen, and C. Hu, High-density racetrack memory based on magnetic skyrmion bags controlled by voltage gates, J. Appl. Phys. **132**, 113901 (2022).

[45] Z. Yu, B. Gong, C. Wei, R. Wang, L. Xiong, L. You, Y. Zhang, S. Liang, Z. Lu, and R. Xiong, Motion of skyrmioniums with negligible deformation in synthetic antiferromagnets, Appl. Phys. Lett. **121**, 012403 (2022).

[46] J. Wang, J. Xia, X. Zhang, X. Zheng, G. Li, L. Chen, Y. Zhou, J. Wu, H. Yin, R. Chantrell, and Y. Xu, Magnetic skyrmionium diode with a magnetic anisotropy voltage gating, Appl. Phys. Lett. **117**, 202401 (2020).

[47] Y. Hu and T. Machon, Stability of highly-twisted skyrmions from contact topology, arXiv:2102.13126.

[48] L. Powalla, M. Birch, K. Litzius, S. Wintz, F. Yasin, L. Turnbull, F. Schulz, D. Mayoh, G. Balakrishnan, M. Weigand, X. Yu, K. Kern, and M. Burghard, Seeding and emergence of composite skyrmions in a Van der Waals magnet, Adv. Mater. **35**, 2208930 (2023).

[49] N. Mehmood, R. Fazal, W. Yadong, T. Guo, Q. Zhang, Z. Hou, G. Xingsen, and J.-M. Liu, Stability phase diagrams and tuning of magnetic skyrmionium and other states, J. Magn. Magn. Mater. **526**, 167706 (2021).

[50] P. C. Carvalho, I. P. Miranda, A. B. Klautau, A. Bergman, and H. M. Petrilli, Complex magnetic textures in $Ni/Ir_n/Pt(111)$ ultrathin films, Phys. Rev. Mater. **5**, 124406 (2021).

[51] M. Mochizuki, X. Z. Yu, S. Seki, N. Kanazawa, W. Koshibae, J. Zang, M. Mostovoy, Y. Tokura, and N. Nagaosa, Thermally driven ratchet motion of a skyrmion microcrystal and topological magnon Hall effect, Nat. Mater. **13**, 241 (2014).

[52] L. Kong and J. Zang, Dynamics of an insulating skyrmion under a temperature gradient, Phys. Rev. Lett. **111**, 067203 (2013).

[53] J. Matsuki and M. Mochizuki, Thermoelectric effect of a skyrmion crystal confined in a magnetic disk, Phys. Rev. B **107**, L100408 (2023).

[54] L. Zhao, Z. Wang, X. Zhang, X. Liang, J. Xia, K. Wu, H.-A. Zhou, Y. Dong, G. Yu, K. L. Wang, X. Liu, Y. Zhou, and W. Jiang, Topology-dependent Brownian gyromotion of a single skyrmion, Phys. Rev. Lett. **125**, 027206 (2020).

[55] J. Barker and O. A. Tretiakov, Static and dynamical properties of antiferromagnetic skyrmions in the presence of applied current and temperature, Phys. Rev. Lett. **116**, 147203 (2016).

[56] B. Heil, A. Rosch, and J. Masell, Universality of annihilation barriers of large magnetic skyrmions in chiral and frustrated magnets, Phys. Rev. B **100**, 134424 (2019).

[57] Y. Liu, G. Yin, J. Zang, J. Shi, and R. K. Lake, Skyrmion creation and annihilation by spin waves, Appl. Phys. Lett. **107**, 152411 (2015).

[58] A. De Lucia, K. Litzius, B. Krüger, O. A. Tretiakov, and M. Kläui, Multiscale simulations of topological transformations in magnetic-skyrmion spin structures, Phys. Rev. B **96**, 020405(R) (2017).

[59] W. Koshibae and N. Nagaosa, Creation of skyrmions and antiskyrmions by local heating, Nat. Commun. **5**, 5148 (2014).

[60] P. F. Bessarab, V. M. Uzdin, and H. Jónsson, Method for finding mechanism and activation energy of magnetic transitions, applied to skyrmion and antivortex annihilation, Comput. Phys. Commun. **196**, 335 (2015).

[61] P. F. Bessarab, Comment on "Path to collapse for an isolated Néel skyrmion," Phys. Rev. B **95**, 136401 (2017).

[62] A. Bernand-Mantel, A. Fondet, S. Barnova, T. M. Simon, and C. B. Muratov, Theory of magnetic field stabilized compact skyrmions in thin-film ferromagnets, Phys. Rev. B **108**, L161405 (2023).

[63] A. Bernand-Mantel, C. B. Muratov, and V. V. Slastikov, A micromagnetic theory of skyrmion lifetime in ultrathin ferromagnetic films, Proc. Natl. Acad. Sci. USA **119**, e2122237119 (2022).

[64] L. D. Landau and E. M. Lifshitz, *Course of Theoretical Physics* (Pergamon, London, 1984), Vol. 8.

[65] F. N. Rybakov and N. S. Kiselev, Chiral magnetic skyrmions with arbitrary topological charge, Phys. Rev. B **99**, 064437 (2019).

[66] I. Dzyaloshinsky, A thermodynamic theory of "weak" ferromagnetism of antiferromagnetics, J. Phys. Chem. Solids **4**, 241 (1958).

[67] T. Moriya, Anisotropic superexchange interaction and weak ferromagnetism, Phys. Rev. **120**, 91 (1960).

[68] R. Zivieri, Statistical thermodynamics of chiral skyrmions in a ferromagnetic material, Materials (Basel) **12**, 3702 (2019).

[69] E. H. Frei, S. Shtrikman, and D. Treves, Critical size and nucleation field of ideal ferromagnetic particles, Phys. Rev. **106**, 446 (1957).
[70] W. F. Brown, Thermal fluctuations of a single-domain particle, Phys. Rev. **130**, 1677 (1963).
[71] J. L. García-Palacios and F. J. Lázaro, Langevin-dynamics study of the dynamical properties of small magnetic particles, Phys. Rev. B **58**, 14937 (1998).
[72] C. J. García-Cervera, Numerical micromagnetics: A review, SeMA J.: Bull. Span. Soc. Appl. Math. **39**, 103 (2007).
[73] G. Da Prato and J. Zabczyk, *Stochastic Equations in Infinite Dimensions*, Encyclopedia of Mathematics and its Applications (Cambridge University, Cambridge, England, 1992).
[74] N. G. van Kampen, Itô versus Stratonovich, J. Stat. Phys. **24**, 175 (1981).
[75] K. Itô, Stochastic integral, Proc. Imp. Acad. **20**, 519 (1944).
[76] N. Romming, A. Kubetzka, C. Hanneken, K. von Bergmann, and R. Wiesendanger, Field-dependent size and shape of single magnetic skyrmions, Phys. Rev. Lett. **114**, 177203 (2015).
[77] A. Siemens, Y. Zhang, J. Hagemeister, E. Vedmedenko, and R. Wiesendanger, Minimal radius of magnetic skyrmions: Statics and dynamics, New J. Phys. **18**, 045021 (2016).
[78] X. S. Wang, H. Y. Yuan, and X. R. Wang, A theory on skyrmion size, Commun. Phys. **1**, 31 (2018).
[79] H.-B. Braun, Fluctuations and instabilities of ferromagnetic domain-wall pairs in an external magnetic field, Phys. Rev. B **50**, 16485 (1994).
[80] A. A. Belavin and A. M. Polyakov, Metastable states of two-dimensional isotropic ferromagnets, JETP Lett. **22**, 245 (1975).
[81] S. Komineas, C. Melcher, and S. Venakides, The profile of chiral skyrmions of small radius, Nonlinearity **33**, 3395 (2020).
[82] S. Komineas, C. Melcher, and S. Venakides, Chiral skyrmions of large radius, Physica D (Amsterdam, Neth.) **418**, 132842 (2021).
[83] A. Bogdanov and A. Hubert, Thermodynamically stable magnetic vortex states in magnetic crystals, J. Magn. Magn. Mater. **138**, 255 (1994).
[84] A. Vansteenkiste, J. Leliaert, M. Dvornik, M. Helsen, F. Garcia-Sanchez, and B. Van Waeyenberge, The design and verification of MuMax3, AIP Adv. **4**, 107133 (2014).
[85] P. Bogacki and L. Shampine, A 3(2) pair of Runge-Kutta formulas, Appl. Math. Lett. **2**, 321 (1989).
[86] E. Feldtkeller, Continuous and singular micromagnetic configurations, IEEE Trans. Magn. **53**, 1 (2017).
[87] C. W. Gardiner, *Handbook of Stochastic Methods for Physics, Chemistry, and the Natural Sciences* (Springer-Verlag, New York, 1997).
[88] R. P. Brent and E. M. McMillan, Some new algorithms for high-precision computation of Euler's constant, Math. Comp. **34**, 305 (1980).
[89] M. I. Freidlin and A. D. Wentzell, *Random Perturbations of Dynamical Systems*, 2nd ed. (Springer, New York, 1998).
[90] J.-V. Kim and J. Mulkers, On quantifying the topological charge in micromagnetics using a lattice-based approach, IOP SciNotes **1**, 025211 (2020).
[91] J. Sampaio, V. Cros, S. Rohart, A. Thiaville, and A. Fert, Nucleation, stability and current-induced motion of isolated magnetic skyrmions in nanostructures, Nat. Nanotechnol. **8**, 839 (2013).
[92] B. Berg and M. Lüscher, Definition and statistical distributions of a topological number in the lattice o(3) σ-model, Nucl. Phys. B **190**, 412 (1981).